



# Temperature fluctuations in the Archean ocean as trigger for varve-like deposition of iron and silica minerals in banded iron formations

Manuel Schad<sup>a</sup>, Maximilian Halama<sup>a</sup>, Brendan Bishop<sup>b</sup>, Kurt O. Konhauser<sup>b</sup>,  
Andreas Kappler<sup>a,\*</sup>

<sup>a</sup> Geomicrobiology, Center for Applied Geosciences, University of Tuebingen, Tuebingen, Germany

<sup>b</sup> Department of Earth and Atmospheric Sciences, University of Alberta, Edmonton, Canada

Received 11 August 2018; accepted in revised form 24 August 2019; Available online 03 September 2019

## Abstract

Banded iron formations (BIFs) are Fe- and Si-rich chemical sediments that were deposited in the oceans throughout the Archean Eon (4.0–2.5 billion years ago; Ga). Despite extensive research pertaining to their composition, mineralogy and depositional settings, the mechanism(s) leading to their characteristic layering is still a matter of debate. Recently, it has been proposed that temperature fluctuations could have acted as the unifying trigger for the precipitation and deposition of Fe(III)-mineral-rich layers mediated by phototrophic Fe(II)-oxidizing bacteria during warm periods and the deposition of silica (SiO<sub>2</sub>)-rich layers by abiotic precipitation of dissolved silica during cold periods. To verify the feasibility of such a mechanism, we conducted laboratory experiments with the marine phototrophic Fe(II)-oxidizing bacterium *Rhodovulum iodolum* under simulated Archean ocean conditions. The temperature was cycled between 26 °C (warm period) and 5 °C (cold period) to mimic temperature fluctuations in the past. Our results showed that *R. iodolum* readily oxidized Fe(II) during warm periods resulting in the formation of an orange-brown Fe(III) mineral layer, whereas it was inactive during cold periods. Conversely, silica largely stayed in solution during warm periods but was precipitated abiotically as an amorphous, gel-like layer during cold periods, enhanced by Si addition that led to Si oversaturation. Most importantly, during Fe(III) mineral precipitation, most silica stayed in solution leading to an independent precipitation of the Fe- and Si-rich layers. This is due to inhibition of silica sorption onto the biogenic Fe-minerals caused by sorption of microbially derived organic matter that contains negatively-charged carboxyl/phosphodiester groups. Analyses of precipitation rates and theoretical sedimentological considerations suggest that this process could explain the banding in BIFs on the microband level and produce sediments of similar thicknesses as found in nature.

© 2019 Elsevier Ltd. All rights reserved.

**Keywords:** Photoferrotrophy; Fe(III) minerals; Abiotic silica precipitation; Temperature cycling; Microbanding; BIF

## 1. INTRODUCTION

Banded Iron Formations (BIFs) are Fe- and Si-rich marine sedimentary deposits which were mainly formed during the Archean and early Paleoproterozoic until ca. 1.8 Ga (Bekker et al., 2010; Bekker et al., 2014; Konhauser et al., 2017a). They are frequently laminated

\* Corresponding author at: Geomicrobiology, Center for Applied Geosciences, University of Tuebingen, Sigwartstrasse 10, D-72076 Tuebingen, Germany.

E-mail address: [andreas.kappler@uni-tuebingen.de](mailto:andreas.kappler@uni-tuebingen.de) (A. Kappler).

on a range of scales that include: (1) macrobands which can be several meters in thickness, (2) mesobands which are usually of a few centimeters in thickness, and (3) microbands which range from the millimeter to sub-millimeter scale and have been proposed to represent an annual cycle of iron and silica precipitation (Trendall and Blockley, 1970). These microbands have also been referred to as chemical varves, where one Fe-rich and one Si-rich layer together represent one year of precipitation (Trendall, 2002). Recently, diurnal nanobands have also been hypothesized (Li, 2014). Compositionally, BIF are characterized by an average redox state of  $\text{Fe}^{2.4+}$  representing their variable Fe(II)- and Fe(III)-bearing mineralogy (e.g. hematite, magnetite, siderite and Fe-silicates; Klein and Beukes, 1992), by a low organic carbon content (<0.5 wt.%) and a Fe-content of 20–40 wt.% and silica-content of 40–50 wt.%  $\text{SiO}_2$  (Trendall, 2002). The most extensive “Superior-type” BIFs are in the Hamersley Range of Western Australia. It is several hundred meters thick,  $10^5 \text{ km}^2$  in aerial extent and contains  $>10^{13} \text{ t}$  of Fe (Isley, 1995; Isley and Abbott, 1999). Due to the lack of current- or wave-related sedimentological features, Superior-type BIFs were likely deposited in depths of more than 100 m (Trendall, 2002) on the continental shelf (Beukes, 1973; Morris and Horwitz, 1983; Klein, 2005).

It is widely accepted that microorganisms were directly or indirectly involved in the initial oxidation and hydrolysis of seawater Fe(II) to form the Fe(III) (oxyhydr)oxide precursor phase to BIF – see Rasmussen et al. (2013, 2015, 2017) for an alternate opinion. The classic model invokes ferric iron precipitation occurring at the interface between oxygenated shallow waters and reduced upwelling iron-rich waters; the oxygen being sourced from cyanobacteria, or their predecessors (Cloud, 1965, 1973). These photoautotrophs would have flourished when nutrients were available and passively induced the precipitation of Fe(III) (oxyhydr)oxides through their metabolic activity. Alternatively, anoxygenic photoautotrophic Fe(II)-oxidizing bacteria (known as photoferrotrophs) could have directly oxidized Fe(II) and coupled this to the fixation of carbon by light energy (Hartman, 1984; Kappler and Newman, 2004). Konhauser et al. (2002, 2017b) suggested that photoferrotrophs might have accounted for most, if not all, Fe(III) deposited in BIF, while iron isotopes in the oldest BIF (the 3.8 Isua Supracrustal Belt in Greenland) suggest the most parsimonious explanation for Fe(II) oxidation was photoferrotrophy (Czaja et al., 2013). Kappler et al. (2005) further showed that the photoferrotrophs could have oxidized all hydrothermally derived Fe(II) before it reached surface waters, even with the simultaneous presence of cyanobacteria in the oxic layer above. The adaptation to low-light conditions would have given photoferrotrophs a competitive advantage over early cyanobacteria which likely inhabited surface waters, especially since cyanobacteria would have had higher phosphate requirements (Jones et al., 2015) and the ferruginous conditions prevailing in the Precambrian ocean might have been toxic to cyanobacteria (Swanner et al., 2015a). Studies that focused on the ecophysiology of photoferrotrophs (Hegler et al., 2008; Posth et al., 2008) support the notion that they could have

prospered in a temperate Precambrian ocean. Moreover, Wu et al. (2014) showed that Fe(II) oxidation rates were not significantly influenced by silica concentrations relevant for the Precambrian ocean. Recent work on modern day analogues for the Precambrian ocean further showed that photoferrotrophs play a key role in their bacterial communities and in the turnover of Fe(II) (e.g. Crowe et al., 2008; Walter et al., 2014; Koeksoy et al., 2015).

One key characteristic of BIFs is the consistency of the alternating Fe- and Si-rich layers. Previous studies suggested that it is possible to correlate microbands over almost 100 km between different cores (Trendall and Blockley, 1970; Ewers and Morris, 1981). If true, the consistency with which these alternating layers were deposited requires a comparable ocean chemistry over much of the depositional basin, and it suggests a unifying trigger for the deposition of Fe-rich and Si-rich layers. The mechanisms suggested for being responsible for BIF banding are divided into primary, secondary or diagenetic. Primary mechanisms imply the precipitation and the banding resulted from some form of periodicity, such as seasonal upwelling of Fe(II)-rich ocean bottom waters onto the continental shelf (e.g. Ewers and Morris, 1981; Morris, 1993). Posth et al. (2008) took the idea one step further by incorporating the role of plankton. They postulated that photoferrotrophs would have been active at temperatures between 20 and 25 °C, for example in summer or during periods of warm climate. This would have resulted in the formation of layers consisting of biogenic Fe(III) (oxyhydr)oxides, while silica would have largely remained soluble. In modern oceans, the seasonal temperature changes may reach up to 6–10 °C, although larger differences might be possible based on local differences in incoming ocean currents and upwelling areas (Pickard and Emery, 1982). Glacial/inter-glacial differences are smaller with between 2–3 °C warming/cooling, however, seasonal differences in temperate regions during these times might have been >12 °C (Pflaumann et al., 2003; MARGO, 2009). Therefore, upon cooling of the ocean (e.g. up to 10–15 °C), either due to incoming cold ocean currents or seasonal changes (Emery et al., 2006), microbial activity would have diminished and amorphous silica could have precipitated abiotically. When the ocean temperature rose again, e.g., in spring, the photoferrotrophs would have resumed their metabolic activity. These estimates are well within estimates given for the Archean ocean, which supposedly was temperate (Krissansen-Totton et al., 2018; Galili et al., 2019) with temperatures ranging from 10–33 °C (Kasting et al., 2006). Thus, this model offers a relatively simple explanation for the wide-scale continuous deposition of Fe-rich and Si-rich micro-bands in BIFs.

Secondary mechanisms invoke mechanical forcing as dominant processes for the alternating deposition of Fe-rich and Si-rich layers in BIF. For instance, Krapež et al. (2003) and Pickard et al. (2004) suggested that BIF precursor sediments might have been transported to a deep-sea BIF depositional basin by either turbidity or deep-sea density currents. Thus, micro-banding in BIF would represent compacted density current lamination. Post-depositional processes during burial and diagenesis

include the compaction of initial BIF sediments resulting in the formation of Fe-rich layers and the vertical escape of the silica which then would have precipitated on top (e.g. Trendall and Blockley, 1970; Dimroth and Chauvel, 1973; Beukes, 1984). Others have suggested that the layers depleted in Fe might represent the post-depositional activity of Fe(III)-reducing bacteria, resulting in remobilization of Fe(II) from the sediment and formation of Si-rich layers (Nealson and Myers, 1990). This could potentially have been controlled by fluctuations in photosynthetic activity with variations in organic matter deposition on the seafloor, resulting in microbial reduction of Fe(III) minerals with this organic matter, its remobilization as Fe(II), and the formation Si-rich layers (Hashizume et al., 2016). Recently, Eglseder et al. (2018) suggested a process where dissolution-precipitation would have resulted in the liberation of hematite particles from their silica matrix. These particles would have accumulated in parallel layers forming microbands, where new hematite particles were formed by non-classical crystallization pathways.

Considering the likelihood that photosynthetic Fe(II)-oxidizing bacteria contributed to BIF, it was our aim to further investigate the primary layering-model involving microbial activity, specifically the fate of Fe(III) and silica during the active growing season. This aspect is not as straightforward as initially proposed in the Posth et al. (2008) model because it has since been suggested that primary Fe(III) minerals could have acted as a shuttle for silica to BIF sediments (Fischer and Knoll, 2009), while other studies have speculated that Fe(II) oxidation in the presence of dissolved silica could have resulted in the formation of a homogeneous, single-phase Fe(III)-silica gel, where Fe and silica are tightly bound and do not form separate silica and Fe(III) (oxyhydr)oxide phases (Doelsch et al., 2001; Percak-Dennett et al., 2011). Zheng et al. (2016) concluded that the primary precipitate of BIFs might therefore have been a Fe(III)-silica gel. Consequently, if the alternating banding of Fe- and Si-rich layers was indeed of primary origin, this would require a mechanism by which the sorption of silica to the primary Fe(III) mineral precipitates can be prevented. Although there is evidence from the rock record in the form of trace element and isotope geochemistry from individual Si- and Fe-rich micro-bands suggesting distinct sources and mechanisms of silica and Fe precipitation (e.g. Frei and Polat, 2007; Bau and Alexander, 2009; Steinhöfel et al., 2010; Viehmann et al., 2014), to date no model has provided a satisfactory answer on why Fe and silica were deposited independently and consistently over large areas.

For our experiments we envisioned an Archean ocean before the development of widespread oxygenic photosynthesis, in which anoxygenic Fe(II)-metabolizing bacteria, such as photoferrotrophs, were primarily responsible for the deposition of BIFs. In order to test whether the model developed by Posth et al. (2008) can be validated with what we now know about Fe-silica interactions, we cultivated the marine photoferrotroph *Rhodovulum iodosum* under conditions relevant for an Archean ocean. We performed precipitation experiments where we followed geochemical parameters, recorded the development of the layering in

the experiments and identified the mineral precipitates formed. Furthermore, in order to elucidate whether cell-derived biomass associated with the Fe(III) minerals results in changes in surface charge or properties, and whether this could prevent co-precipitation of Fe(III) minerals and amorphous silica, we conducted zeta-potential ( $\zeta$ -potential) measurements and potentiometric titrations on the cell-Fe(III)-mineral aggregates formed during microbial Fe(II) oxidation. Finally, in order to evaluate how the tested model could have contributed to the deposition of BIFs, we took our experimental data and extrapolated them to the ca. 2.5 billion-year-old Hamersley Group in Western Australia as a model depositional basin for BIF.

## 2. MATERIALS AND METHODS

### 2.1. Source of microorganisms, culturing medium and growth conditions

*R. iodosum* is a marine photoferrotroph belonging to the purple bacteria and placed amongst the  $\alpha$ -Proteobacteria. It was first isolated from a mud flat of the Jadebusen (North Sea) (Straub et al., 1999). The culture used was obtained from the Deutsche Sammlung von Mikroorganismen und Zellkulturen (DSMZ) in Germany (DSM 12328T) and kept in our laboratory collection for several years. Although it survives and grows at a wide range of temperatures between 10 and 35 °C, it has a relatively narrow optimum where it shows the highest Fe(II) oxidation activity between 20 and 25 °C.

*R. iodosum* was cultivated on marine phototroph medium which was prepared as outlined in Wu et al. (2014), but with the following modifications: (1) To simulate Archean seawater silica concentrations, 0.5684 g L<sup>-1</sup> Na<sub>2</sub>SiO<sub>3</sub>·9 H<sub>2</sub>O was added to achieve a final silica concentration of 2 mM (Maliva et al., 2005). (2) Instead of 22 mM sodium bicarbonate, we added 30 mM as primary buffer and the pH was adjusted to 7.0. (3) No FeCl<sub>3</sub> was added to the trace metal solution, and instead Fe(II) was added as an anoxic and sterile 1 M FeCl<sub>2</sub>·4 H<sub>2</sub>O stock solution (Hegler et al., 2008) at an initial concentration of 5 mM. Although this initial Fe(II) concentration is higher than the Fe(II) concentrations assumed for the Archean ocean (up to 0.5 mM; Holland, 1973; Morris, 1993), this high concentration was necessary to perform the experiments within a reasonable timeframe. (4) The medium was filtered once after the addition of Fe(II) to remove any Fe(II)-carbonate and -phosphate precipitates formed. The filtered medium was then transferred into 1L SCHOTT glass bottles and the headspace exchanged with N<sub>2</sub>/CO<sub>2</sub> (90:10, v/v) for 5 min. Therefore, in order to achieve maximum removal of minerals that are expected to form from the added Fe(II), phosphate and bicarbonate, the medium was placed at 5 °C for at least 48 h. Following the formation of greenish-grey precipitates (likely siderite or vivianite; Hohmann et al., 2009), after 48 h, the pH of the medium was adjusted to 6.8 to simulate the circumneutral pH of the Archean seawater (Halevy and Bachan, 2017). Any forming precipitates were removed by filtration (Millipore filter, 0.22 μm) in an anoxic glovebox

(100% N<sub>2</sub> atmosphere), and the headspace was again exchanged for N<sub>2</sub>/CO<sub>2</sub> (90:10, *v/v*). Filtration of the medium resulted in a removal of ~30% of the initially added Fe<sup>2+</sup> and ~31% of the added Si(OH)<sub>4</sub>. Consequently, the resulting starting concentration in the experiment was ~3.5 mM Fe<sup>2+</sup> and ~1.4 mM monomeric silica. For stock cultures of *R. iodosum* 25 mL of medium were transferred into 58 mL serum bottles. Stock cultures were inoculated with 4% inoculum and incubated at 26 °C in a light incubator with a 40-W incandescent light bulb.

## 2.2. Experimental set-up

In our experiments we aimed at simulating an Archean ocean prior to the development of widespread oxygenic photosynthesis in which anoxygenic photosynthetic Fe(II)-oxidizing bacteria would have accounted for most, if not all, Fe(II) being oxidized. To test whether temperature cycles can couple the biotically mediated precipitation of Fe(III) mineral layers during warm periods to the abiotic precipitation of silica during cold periods, we conducted precipitation experiments where we cycled the temperature between 26 °C and 5 °C – the temperature extremes exhibited by this species. This temperature change of 21 °C is within the temperature range that was suggested for ancient oceans (between 10 and 33 °C; [Kasting et al., 2006](#)), but crucially from an experimental perspective, these temperatures were chosen to demonstrate the feasibility of this mechanism within a reasonable timeframe. In total we simulated two warm periods (26 °C in the light) and one cold period (5 °C in the dark) over a period of 168 days in the main experiment. We also performed experiments specifically designed to investigate: (1) *R. iodosum*'s ability to oxidize Fe(II) at low temperatures, (2) *R. iodosum*'s ability to commence Fe(II) oxidation once it had been exposed to low temperatures, and (3) the effect of low temperatures and silica oversaturation on the chemical precipitation of amorphous silica.

### 2.2.1. First warm period – Fe(II) oxidation prior to silica precipitation

The main temperature cycling experiments were run in biotic triplicates with one additional abiotic (not inoculated) control. The abiotic control was set up to emphasize the key role of microbial Fe(II)-oxidizing activity and temperature in triggering the alternating deposition of Fe- and Si-rich layers by showing that in the absence of living cells no Fe(III) (oxyhydr)oxide formation will take place. 18 mL of filtered Fe(II)- and silica-containing medium (as described in [Section 2.1](#)) were transferred into 20 mL headspace vials in an anoxic glovebox (100% N<sub>2</sub>), stoppered with butyl rubber stoppers, brought out of the glovebox and the headspace exchanged for N<sub>2</sub>/CO<sub>2</sub> (90:10, *v/v*).

To initiate the biogenic precipitation of Fe(III) minerals, the biotic triplicates were inoculated with 5% (approximately  $7.5 \times 10^7$  cells mL<sup>-1</sup>) of a *R. iodosum* culture pre-grown on filtered medium containing 3.5 mM Fe(II) and 1.4 mM of silica (as described in [Section 2.1](#)) after an equal amount of medium was removed. The removed medium was subsequently used for Fe<sup>2+</sup> and monomeric silica quan-

tification. The cultures were pre-grown in the presence of silica to adapt them to Si-rich conditions. All headspace vials were placed in a light incubator at 26 °C and sampled every 5–6 days for Fe<sup>2+</sup> and monomeric silica quantification as described below. Once all Fe(II) was oxidized, an aliquot of medium was removed from each vial so that 8 mL remained. The supernatant removed was then used to quantify the remaining Fe<sup>2+</sup> and monomeric silica. The vials were subsequently refilled with filtered Fe(II)- and silica-containing medium in an anoxic glovebox (100% N<sub>2</sub>) to 18 mL, where care was taken to not disturb the already sedimented mineral layer. The headspace was exchanged for N<sub>2</sub>/CO<sub>2</sub> (90:10, *v/v*), each vial was sampled again for Fe<sup>2+</sup> and monomeric silica concentrations and then placed at 26 °C in the light. These steps were repeated until a clearly visible ca. 0.5–1 mm thick Fe(III) mineral layer had developed ([Fig. 1A](#)).

### 2.2.2. Cold period – abiotic silica precipitation

Once a sufficiently thick Fe(III) mineral layer had developed in the main experiment, monomeric silica (to a final concentration of ca. 4 mM) was added from a 50 mM Na<sub>2</sub>-SiO<sub>3</sub>·9 H<sub>2</sub>O stock solution (~pH 12.8) to test whether amorphous silica precipitation would already take place at this concentration ([Tab. A.1](#), day 35). The monomeric silica solution was freshly prepared, adjusted to circumneutral pH using 1 M HCl in an anoxic glovebox (100% N<sub>2</sub> atmosphere) and 1.44 mL immediately added to the headspace vials. The neutralization was necessary to maintain the neutral pH of the medium and prevent the added monomeric silica from immediately being precipitated upon addition to the medium. The volume of 18 mL in the headspace vials was maintained by removing an amount of medium equal to the amount of silica solution added while also accounting for the volume removed during sampling. The removed medium was used for Fe<sup>2+</sup> and monomeric silica quantification and pH monitoring. After addition of the silica, the headspace vials were given 1 hour to equilibrate at room temperature in the light, the headspace was exchanged for N<sub>2</sub>/CO<sub>2</sub> (90:10, *v/v*) and sampled again for Fe<sup>2+</sup> and monomeric silica quantification. The headspace vials were then placed at 5 °C in the dark.

Although amorphous silica precipitation would have been expected based on known solubility values (1.3 mM at 5 °C; [Gunnarsson and Arnórsson, 2000](#)), no amorphous silica precipitation was observed at day 54. This lack of amorphous silica precipitation is potentially attributed to slow silica precipitation kinetics ([Krauskopf, 1956](#) and references therein) or a lack of nucleation sites necessary for initiating the polymerization and precipitation of silica. Therefore, to identify the concentration of monomeric silica necessary to complete the experiment within a reasonable timeframe, we varied the concentration of the added monomeric silica ([Table A.1](#)), and from day 93 onwards, 8 mM monomeric silica were added repeatedly once the concentration dropped below 2 mM to create the amorphous silica layer. Care was taken to not disturb any layering that had already developed. During the entire time the headspace vials were kept at 5 °C in the dark. The sampling frequency for Fe<sup>2+</sup> and monomeric silica quantification was adjusted

from initially 7 days to 3 or 4 days to better resolve the development of the monomeric silica concentration.

Additionally, we investigated (1) how oversaturation with regards to amorphous silica would influence silica precipitation at low temperatures and (2) how the presence of cells, Fe(II) and light would influence the amorphous silica layer being formed. All complementary experiments were performed using the silica-containing marine phototroph medium in the same headspace vials using the general experimental setup. To answer the first question, Fe(II)-free marine phototroph medium was used. Fe(II) was omitted in this particular experiment in order to rule out any effect on silica precipitation by interaction of Fe(II) and silica during the formation of Fe(II)-silicates. This allowed to specifically determine the influence of temperature on silica precipitation. The experiment was divided into four setups each consisting of triplicates. To half of the setups neutralized monomeric silica was added to a final concentration of 8 mM as described before. The other half did not receive any additional silica and thus only contained approximately 1.4 mM monomeric silica. For each silica concentration half of the setups were incubated at 26 °C and light and the other half at 5 °C and light. Samples for dissolved monomeric silica quantification were taken before addition of additional monomeric silica and directly after addition of monomeric silica. During the first 12 h of the experiment samples were taken every 2–4 h, after 24 h, and every 2–3 days thereafter.

To answer the second question, the Fe(II)-containing marine phototroph medium was used. The experiment was set up as biotic triplicates containing 5% (0.9 mL) *R. iodosum*, pre-grown on Fe(II)- and silica-containing medium, and one abiotic (non-inoculated) control. Neutralized monomeric silica was added to all headspace vials to achieve a final concentration of 8 mM. All headspace vials were incubated at 5 °C and light. Samples for Fe<sup>2+</sup> and dissolved monomeric silica quantification were taken before addition of cells and monomeric silica and directly afterwards. Thereafter, samples were taken continuously every 2–3 days.

Furthermore, we determined whether *R. iodosum* would be able to oxidize Fe(II) under low temperature (5 °C) conditions. The experiment consisted of a biotic triplicate containing 5% (0.9 mL) *R. iodosum*, pre-grown on Fe(II)- and silica-containing medium, and one abiotic (non-inoculated) control and was incubated continuously under light and at 5 °C. Samples for Fe<sup>2+</sup> and dissolved monomeric silica quantification were taken immediately before and directly after the addition of *R. iodosum* cells and every 2–3 days thereafter.

### 2.2.3. Second warm period – Fe(II) oxidation following silica precipitation at low temperatures

Once a clearly visible 2–3 cm thick amorphous silica layer had developed in the main temperature cycling experiment, an aliquot of the supernatant (medium) was removed so that 14.1 mL remained in each headspace vial. The removed volume was used for Fe<sup>2+</sup> and monomeric silica quantification and pH monitoring. For the precipitation of the second Fe(III) mineral layer, 3.15 mL of filtered

Fe(II)- and silica-containing medium was added to the biotic triplicates and 4.05 mL to the abiotic controls in an anoxic glovebox (100% N<sub>2</sub> atmosphere). The headspace was exchanged for N<sub>2</sub>/CO<sub>2</sub> (90:10, v/v), all headspace vials were sampled again for Fe<sup>2+</sup> and monomeric silica, and the biotic triplicates were re-inoculated with 5% (0.9 mL) of a pre-grown *R. iodosum* stock culture which resulted in approximately  $7.5 \times 10^7$  cells mL<sup>-1</sup> (Wu et al., 2014). The medium was exchanged to balance the loss of nutrients during the previous oxidation step, the dilution of the medium during the addition of the monomeric silica solution and supply new Fe(II) for growth of *R. iodosum*. A re-inoculation with new *R. iodosum* cells was deemed necessary as prolonged cold temperature and darkness (79 days), as well as dilution of the medium during the addition of the silica solution, potentially damaged the cells so that a fraction of them were possibly no longer viable. To simulate the second warm period all headspace vials were placed in a light incubator at 26 °C and sampled every 3–4 days for Fe<sup>2+</sup> and monomeric silica quantification. 3 mL of medium were repeatedly exchanged as described before (including Fe<sup>2+</sup> and monomeric silica quantification as well as pH monitoring) once the Fe(II) oxidation was completed until a clearly visible Fe(III) mineral layer had developed.

Finally, to determine whether *R. iodosum* would be able to recover from cold stress, we performed an experiment with Fe(II)- and silica-containing marine phototroph medium. The experiment was set up as biotic triplicates containing 5% (0.9 mL) *R. iodosum* pre-grown on Fe(II)- and silica-containing medium, with one abiotic (not inoculated) control. The headspace vials were incubated at 26 °C and light until approximately half of the initial Fe(II) was oxidized. Thereafter, the headspace vials were transferred to 5 °C and light, kept under these conditions for 10 days, and then transferred back to 26 °C and light where they were incubated until all Fe(II) was oxidized. Samples for Fe<sup>2+</sup> and dissolved monomeric silica were taken before addition of *R. iodosum* and directly after inoculation. Thereafter, samples were taken every 2–3 days.

### 2.3. Fe analysis and calculation of maximum oxidation rates

For Fe<sup>2+</sup> quantification 100 µL of sample was taken from the headspace vials under a constant N<sub>2</sub>/CO<sub>2</sub> (90:10, v/v) stream, fixed in 900 µL 1 M HCl and stored at 5 °C until analysis. For the quantification of Fe<sup>2+</sup> the ferrozine assay was used (Stookey, 1970). The absorbance at 562 nm was measured with a microtiter plate reader (Multiskan GO Microplate Spectrophotometer with internal software (SkanIT RE for Multiskan GO 3.2)).

The maximum oxidation rates were determined by linear regression analysis through the steepest 2 or when possible, steepest 3 points of the Fe<sup>2+</sup> curve at a given time point.

### 2.4. Silica analysis

For silica analysis 50 µL of sample were taken from the headspace vials under a constant N<sub>2</sub>/CO<sub>2</sub> (90:10, v/v) stream, diluted either 1:20 or 1:40 with MilliQ® water to

not exceed the maximum concentration of 80  $\mu\text{M}$  for the assay and measured as soon as possible after sampling. For quantification of monomeric silica, a modified protocol of the molybdenum blue method from Strickland and Parsons (1972) was used. To 1 mL of diluted sample 40  $\mu\text{L}$  acid molybdate solution was added, mixed by shaking and allowed to react for 15 minutes at room temperature. Thereafter, 40  $\mu\text{L}$  of oxalic acid were added, mixed by shaking and 20  $\mu\text{L}$  of ascorbic acid added immediately afterwards. The blue color was allowed to develop for 60 min at room temperature. 200  $\mu\text{L}$  of sample were then measured spectrophotometrically at 810 nm in black-walled micro-titer plates using a Multiskan GO Microplate Spectrophotometer with internal software (SkanIT RE for Multiskan GO 3.2).

### 2.5. Zeta-potential ( $\zeta$ -potential) measurements

*R. iodosum* was cultivated as described above in 100 mL serum bottles containing 50 mL anoxic marine phototroph medium without additional silica. To compare the  $\zeta$ -potential of biogenic Fe(III) minerals produced by the Fe(II)-oxidizing strain *R. iodosum* to abiotically precipitated Fe(III) minerals, pressurized 0.22  $\mu\text{m}$ -filtered air (with 21%  $\text{O}_2$ ) was added to serum bottles with the same Fe(II)-containing medium but not inoculated with *R. iodosum* to oxidize the Fe(II) abiotically leading to the precipitation of abiogenic Fe(III) minerals.

Samples of biogenic and abiogenic Fe(III) minerals were diluted with 10 mM HEPES-buffered MilliQ<sup>®</sup> water, which was adjusted to pH 6.8 in order to have the same pH as in the initial medium. To test the influence of the geochemical composition of the marine medium on the  $\zeta$ -potential values, abiogenic ferrihydrite (Schwertmann and Cornell, 2008) and biogenic Fe(III) minerals produced by *R. iodosum* were mixed with a modified version of the above described marine phototroph medium which was mixed at different ratios with 10 mM HEPES buffered MilliQ<sup>®</sup> water (medium only, 10:1, 1:1, 1:10 and MilliQ<sup>®</sup> water only). For the modified marine phototroph medium, the medium was prepared under air, no medium additives were added, the bicarbonate buffer was replaced by a 10 mM HEPES buffer, and the pH was adjusted to 6.8. All measurements were conducted using a Zetasizer Nano ZSP (Malvern, Herrenberg, Germany) with Zetasizer Nano Series disposable folded capillary cells (DTS1070; Malvern, Herrenberg, Germany).

### 2.6. Potentiometric titrations of Fe(III) mineral-cell aggregates

For potentiometric titrations, *R. iodosum* was cultivated as described above in silica-free medium. Upon completion of Fe(II) oxidation (determined by the Ferrozine method), the remaining medium including free cells was removed anoxically after shaking and inverting the culture and allowing the cell-Fe(III)-mineral aggregates to settle. Thereafter, fresh Fe(II)-free medium was added, the bottle was shaken gently, the cell-mineral-aggregates allowed to re-settle, and the medium supernatant removed again. This washing step was repeated twice to remove any free cells

from solution in order to only have cell-Fe(III)-mineral aggregates for the titrations. After the last washing step, the samples were suspended in 0.01 M  $\text{NaNO}_3$  and centrifuged for 10 min at 10,000 g, after which the  $\text{NaNO}_3$  was decanted and wet mass of sample was determined. Then, 0.075 g of the cell-mineral aggregates were suspended in 30 mL of 0.01 M  $\text{NaNO}_3$  for a concentration of 2.5  $\text{g L}^{-1}$  (wet mass) and purged with  $\text{N}_2$  gas for 15 min prior to and during the titration in order to establish and maintain a  $\text{CO}_2$  free environment. The titrations were performed on a Metrohm Titrando 905 using a Metrohm pH probe calibrated to pH 4, 7, and 10 using commercially available buffers (Fisher Scientific). Initially, the solution was acidified to pH 3 using 0.1 M HCl, followed by an “up” titration where the pH of the solution was increased to pH 9 by incrementally adding aliquots of 0.1 M NaOH, with the amount of titrant and pH recorded with each addition. Once pH 9 was achieved, a “down” titration was performed to return the pH to 3 by adding aliquots of 0.1 M HCl to test the reversibility of proton binding and to observe for any hysteresis due to dissolution of the aggregates. All titrations were performed using “dynamic mode” where the titrator adds a variable amount of titrant depending on the instantaneous buffering capacity of the system, with additions only being made once the pH electrode achieved a stability of 0.2  $\text{mV s}^{-1}$ .

The titration data was evaluated in terms of the concentration of base added to the system and modeled using a least-squares optimization method to solve for both site densities and  $\text{pK}_a$  values within a fixed interval using FITEQL v 4.0 (Herbelin and Westall, 1999). Models employing 2–4 proton-binding sites were tested in FITEQL, with a 2-site model having the best fit to the experimental titration data.

### 2.7. $^{57}\text{Fe}$ Moessbauer spectroscopy

Samples for Fe(III) mineral identification were taken from the experiments as liquid mineral suspensions and filtered through 0.45  $\mu\text{m}$  Luer-lock filters and fixed on Kapton tape. The samples were loaded into a closed-cycle exchange gas cryostat (Janis cryogenics). Spectra were collected at 77 K and 5 K in transmission geometry using a constant acceleration drive system (WissEL) in the Geomicrobiology group at Center for Applied Geosciences, University of Tuebingen. A  $^{57}\text{Co}$  source embedded in a Rhodium matrix was used as  $\gamma$ -radiation source. The spectra were calibrated against a 7  $\mu\text{m}$  thick  $\alpha$ - $^{57}\text{Fe}$  foil at room temperature. The RECOIL software suite (University of Ottawa, Canada) was used for the calibration and spectra modeling using Voigt-based line shapes was performed (Rancourt and Ping, 1991). The Lorentz half-width-half-maximum was kept constant at 0.14  $\text{mm s}^{-1}$  as determined by using the minimum line width of the third and fourth peak of the calibration foil in the models. The Gauss' sigma parameter was used to account for line broadening. The relative proportion of the areas covered by each doublet and sextet of the total spectrum is corresponding to the relative abundance of Fe in a particular crystal lattice site.

## 2.8. $\mu$ XRD measurements

For  $\mu$ XRD measurements an aliquot of the mineral suspensions was sampled from the experiment, the cell-Fe(III)-mineral aggregates were harvested by centrifugation (1761 g) and vacuum-dried. A small aliquot of this mineral powder was put on a silicon wafer.  $\mu$ XRD measurements were conducted using a 2D-Microdiffractometer (Bruker D8 Discover with GADDS,  $\mu$ -XRD<sup>2</sup>, Bruker AXS GmbH, Karlsruhe, Germany) available in the Geoscience Department at the University of Tuebingen. The instrument was equipped with a Co-anode as X-ray source with a Co-K $\alpha$  wavelength of 1.79030 Å, a primary graphite monochromator and a 2D detector with 40° angle cover (Bruker Vântec 500, Bruker AXS GmbH, Karlsruhe, Germany). Reflection patterns were collected for 120 seconds per angle setting. Reflection pattern analysis and mineral identification was carried out using the Match!© program for phase identification from powder diffraction (Match!, Crystal Impact, Bonn, Germany).

## 2.9. Scanning electron microscopy (SEM)

For SEM imaging, *R. iodosum* was cultivated as previously described in 100 mL serum bottles containing either silica-free or silica-containing marine phototroph medium. In order to compare the morphology of the cell-Fe(III) mineral aggregates formed by *R. iodosum* to abiotically precipitated Fe(III) minerals, pressurized, 0.22  $\mu$ m-filtered air (21% oxygen) was added to serum bottles with the same Fe(II)-containing medium but not inoculated with *R. iodosum*. Samples for SEM were fixed in glutaraldehyde (final concentration 2.5%) overnight, washed twice with MilliQ® water, and mounted on Poly-L-lysine covered glass slides. The samples were prepared by serial dehydration with ethanol (30%, 70%, 95%, each 5 minutes and 2x 100%, each 30 minutes), treated with hexamethyldisilazan (HMDS, 2 times 30 seconds) and dried by evaporation at room temperature and ambient pressure (Zeitvogel et al., 2017). Samples were coated with a ~15 nm Pt-layer using a Balzers Union Med 010 (Bal-Tec, Balzers, Liechtenstein) sputter coater. SEM analysis was performed at the Center for Applied Geosciences, University of Tuebingen, using a LEO 1450 VP (Zeiss) equipped with an Everhart-Thornley SE-Detector. Secondary electron (SE) imaging was performed at an acceleration voltage of 7 kV with a working distance of 8 mm. The pressure was targeted at  $8 \times 10^{-6}$  mbar. No elemental analysis by EDS was performed.

## 2.10. Fe(III) mineral aggregate size analysis

For Fe(III) mineral aggregate size determination, the ImageJ software was used to analyze the aggregates visualized in SEM micrographs. To randomize the particles counted, horizontal, vertical and diagonal lines were drawn from the top left corner of the picture and all aggregates along these lines measured. For all aggregates the distance between the two points the farthest away from each other were measured. In order to obtain some statistical signifi-

cance at least 100 aggregates were analyzed. It has to be noted that aggregate size analysis by SEM is a 2D technique and does not consider potential differences in size in the z-axis.

## 2.11. Modelling of mineral saturation states and aqueous speciation

Geochemical modelling was performed for the low-temperature stage of the precipitation experiments in order to determine the aqueous speciation of silica and compare the mineral saturation states of amorphous silica and greenalite under the given silica and Fe(II) concentrations and geochemical composition of the medium used in the experiment. For equilibrium speciation modelling Visual MINTEQ vs. 3.1 was used employing a solubility product for greenalite of  $\log K_{sp} = 27.70$  calculated based on Tosca et al. (2016).

## 3. RESULTS

### 3.1. Development of Fe(III) and silica mineral layers at fluctuating temperatures

In order to demonstrate the alternating precipitation of Fe(III) and silica minerals, we incubated Fe(II)- and silica-containing medium with the phototrophic Fe(II)-oxidizing bacterium *Rhodovulum iodosum* and cycled the temperature between 26 °C and 5 °C. The basic idea of the experimental setup was (1) to investigate how the presence of silica concentrations near the saturation state of amorphous silica (ca. 2 mM) affect microbial Fe(II) oxidation at warm temperatures and whether this would affect the formation of Fe(III) mineral layers, and (2) to explore the effect of lowering the temperature on the precipitation of silica in the presence of high concentrations of dissolved Fe<sup>2+</sup> and how lowering the temperature would affect the activity of *R. iodosum*. For silica precipitation at low temperatures, silica concentrations above the saturation limit of ca. 2 mM were necessary, in our case ca. 8 mM, to overcome the kinetic limitations for precipitation and to observe precipitation in experimentally reasonable timeframes of several weeks. Similarly, higher Fe<sup>2+</sup> concentrations of 2–3 mM, compared to the ca. 0.5 mM Fe<sup>2+</sup> concentration assumed for the Archean ocean, were necessary to precipitate a sufficient quantity of Fe(III) minerals within the experimental timeframe.

Photos of the precipitating Fe mineral and amorphous silica layers were taken in order to record the banding development. The activity of the phototrophic Fe(II)-oxidizing bacterium *R. iodosum* at 26 °C in the light resulted in the formation of orange-colored Fe(III) mineral precipitates. After 54 days, during which fresh Fe(II)- and silica-containing medium had been added 4 times to simulate constant input in ancient oceans of Fe<sup>2+</sup> from hydrothermal activity and silica from the continents (Hamade et al., 2003), an approximately 1 mm thick Fe(III) mineral layer developed (Fig. 1A). During the same time the abiotic (not inoculated) setup remained colorless and only a minor amount of pale greyish-green precipitates formed (inset Fig. 1A). This corresponded to a removal of aqueous Fe(II) of only 7% compared

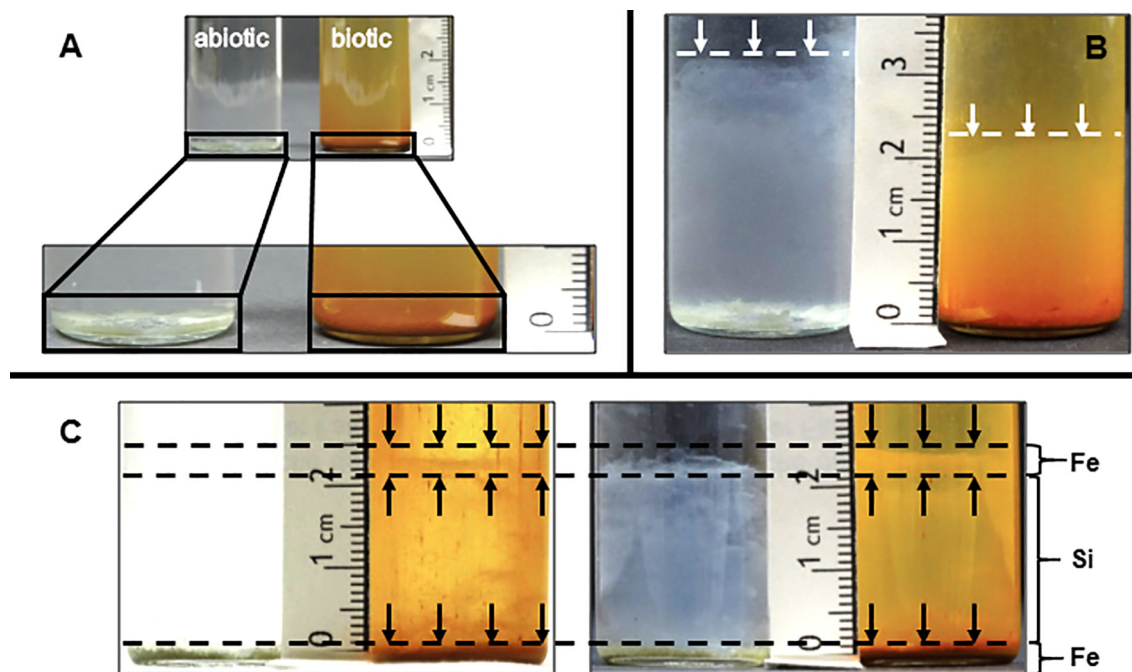


Fig. 1. Development of iron- and silica-layering over time. (A) Shows microbially mediated deposition of a Fe(III) mineral layer by the activity of the phototrophic Fe(II)-oxidizer *R. iodosum* at 26 °C compared to the abiotic setup. The upper picture in (A) shows Fe(II) oxidation and formation of Fe(III) minerals which is evident by the development of orange-colored minerals after 43 days. The lower picture in (A) shows close-ups that demonstrate the precipitation of the orange Fe(III) minerals in the biotic but not in the abiotic setups. (B) Shows the abiotic precipitation of amorphous silica at 5 °C after 126 days in the biotic setups (right) as well as in the abiotic, not-inoculated setup (left). The white dashed line and arrows indicate the upper limit of the amorphous silica layer. Please note that the white band in the biotic setup is difficult to see in the right photograph due to the orange minerals that stick to the glass wall. (C) Shows the deposition of an orange-colored Fe(III) mineral layer (2.1–2.5 cm) on top of the previously precipitated amorphous silica layer (0.1–2.1 cm) in the biotic setup after 168 days. The precipitation of Fe(III) minerals in biotic setups is mediated by *R. iodosum* at 26 °C during a second warm period. A bright (left picture) and dark (right picture) background were chosen in order to better visualize the difference between the Fe and silica layers. Respective layers are marked by black dashed lines, arrows and braces with labelling.

to the amount that was oxidized and precipitated by the photoferrotrophs. After the development of the Fe(III) mineral layer by day 54, more monomeric silica was added to all setups which were then transferred to 5 °C resulting in the supersaturation of the medium with respect to amorphous silica. After 126 days, a clearly defined amorphous silica layer had developed (Fig. 1B). This amorphous silica layer was visible in both the biotic vials that contained *R. iodosum* cells, as well as in the abiotic setups. Following the addition of new medium, re-inoculation of the biotic setups with *R. iodosum*, and the transfer back to 26 °C and light, caused a second Fe(III) mineral layer to precipitate on top of the amorphous silica layer. This layer was again visible as orange-colored Fe(III) minerals in the biotic setups (Fig. 1C). The alternating layers of Fe(III) minerals and amorphous silica remained stable and clearly distinct on a macroscopic level until the end of the experiment, although the thickness of the silica layer decreased slightly from approximately 3 cm to 2.5 cm due to density-driven compaction.

### 3.2. Fe(III) mineral formation by microbial phototrophic Fe(II) oxidation and abiotic silica precipitation

In addition to the physical changes during the deposition of alternating Fe(III)- and silica-rich layers, we also

followed the underlying changes in the geochemistry of our experimental solution. Specifically, we measured changes in concentrations of the dissolved species, Fe<sup>2+</sup> and monomeric silica.

During the first warm incubation period, *R. iodosum* oxidized ca. 2.0–2.5 mM of dissolved Fe<sup>2+</sup> within 4–7 days (Fig. 2, upper panel until day 35) yielding initial average Fe(II) oxidation rates of ca. 0.3 mM d<sup>-1</sup> (between day 0 and 13) and maximum Fe(II) oxidation rates of 0.6 mM d<sup>-1</sup>. Fe(II) removal from solution mediated by *R. iodosum* was >96%. Although there was some removal of monomeric silica from solution together with the Fe(III) minerals during Fe(II) oxidation, approximately 1.0 mM monomeric silica stayed in solution all the time (Fig. 2). No Fe(II) oxidation was observed in the abiotic control during the first warm period as indicated by the absence of orange-colored precipitates (Fig. 1A).

During the cold period between days 54 and 133 (Fig. 2), monomeric silica was added in 5 spikes to the biotic setups, each resulting in measured monomeric silica concentrations of >4 mM (day 99). Concentrations of monomeric silica decreased quickly (within 3–6 days) to an overall average of 1.7 mM (Fig. 2). The average monomeric silica concentration immediately before adding a new silica spike was 1.6 mM. Maximum removal rates of monomeric silica

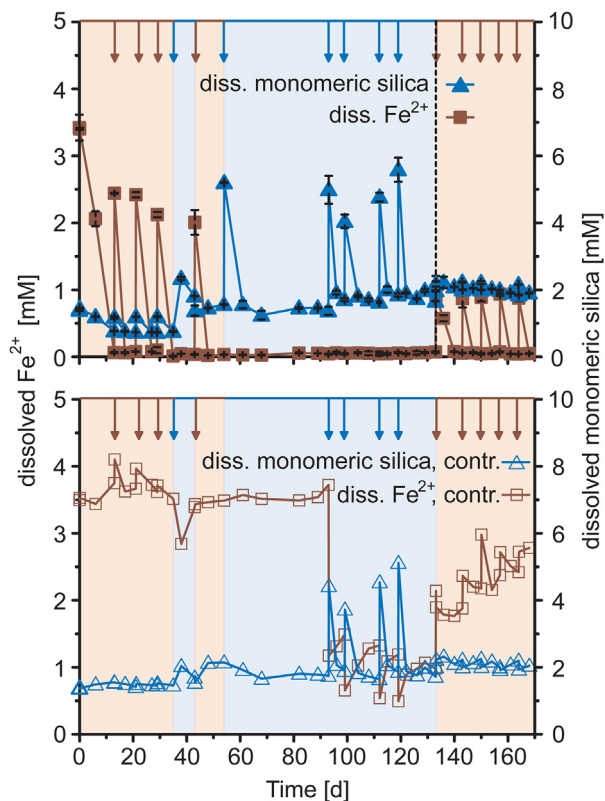


Fig. 2. Variations in dissolved  $\text{Fe}^{2+}$  and monomeric silica concentrations over time during temperature cycles under simulated Archean ocean conditions. The top panel shows the biotic setups, while the bottom panel shows the abiotic (non-inoculated) setup. Orange arrows mark removal of supernatant and addition of new microbial growth medium with ca. 3.5 mM of  $\text{Fe}^{2+}$  and ca. 1.4 mM of monomeric silica. Blue arrows mark addition of monomeric silica solution. Orange shaded areas mark incubation at 26 °C and light. Blue shaded areas mark incubation at 5 °C in the dark. Vertical black dashed line marks re-inoculation with *R. iodosum* in the biotic replicates. Data shown for biotic setups are the mean of triplicates  $\pm$  standard deviation. Data of abiotic controls are single measurements. (For interpretation of the references to color in this figure legend, the reader is referred to the web version of this article.)

ranged from 0.3–0.5  $\text{mM d}^{-1}$ . The  $\text{Fe}^{2+}$  concentration in the biotic setup remained at approximately 0 mM as expected due to the absence of fresh  $\text{Fe}^{2+}$  addition. The monomeric silica concentrations in the abiotic control essentially equaled those in the biotic setups. The  $\text{Fe}^{2+}$  concentration in the abiotic setup (that was ca. 3.5–3.7 mM before silica addition) decreased significantly after the first addition of monomeric silica from 3.5 mM to 1.2 mM. This is likely due to the removal of Fe(II)-containing medium prior to the addition of neutralized monomeric silica and potentially the precipitation of some Fe(II)-silicates; it further decreased during the subsequent additions of monomeric silica to a value of ca. 1 mM. Prior to each addition of neutralized monomeric silica solution between 8% and 40% of the existing solution was removed. Consequently, at the end of the cold phase only about 34% of the initial solution was still present in each vial. Similarly, as proposed

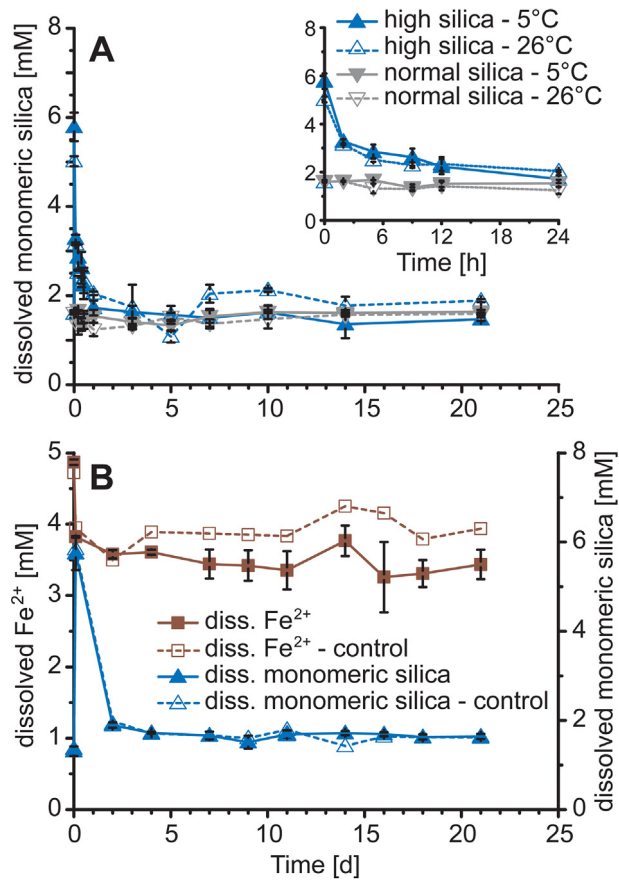


Fig. 3. Development of dissolved monomeric silica concentration over time during: (A) silica precipitation kinetics experiments at 5 °C and 26 °C in light and (B) dissolved  $\text{Fe}^{2+}$  and monomeric silica concentrations during silica precipitation in the presence of *R. iodosum*, dissolved  $\text{Fe}^{2+}$  at 5 °C and light. The insert in (A) shows the development of dissolved monomeric silica during the first 24 h. Data shown in (A) are the mean from triplicates  $\pm$  standard deviation. In (B) data for biotic setups are the mean from triplicates  $\pm$  standard deviation while the data for the abiotic (non-inoculated) control represent single measurements.

above,  $\text{Fe}^{2+}$  would have been removed from solution to a final concentration of approximately 1.2 mM. All other nutrients and solutes were diluted in a similar manner.

Since a high degree of silica oversaturation was necessary to overcome the kinetic limitation of amorphous silica precipitation in the main experiment, we performed additional experiments to: (1) compare the kinetics of silica precipitation at different silica concentrations and temperatures to determine the effect of amorphous silica oversaturation during the cold period, and (2) determine the combined influence of Fe(II), cells and light on amorphous silica precipitation during the cold period. The silica precipitation kinetics experiments (Fig. 3, panel A) showed that at elevated initial monomeric silica concentrations (8 mM), 74.5% (at 5 °C) and 80.8% (at 26 °C) of the silica were removed during the first 24 h of the experiment. Monomeric silica polymerization/removal rates showed no significant differences for 5 °C and 26 °C (0.56

$\pm 0.09 \text{ mM h}^{-1}$  and  $0.48 \pm 0.02 \text{ mM h}^{-1}$ , respectively;  $p = 0.2073$ ). However, the final equilibrium concentration at day 21 differed significantly ( $p = 0.0001$ ) with  $1.47 \pm 0.04 \text{ mM}$  at  $5^\circ\text{C}$  and  $1.89 \pm 0.03 \text{ mM}$  at  $26^\circ\text{C}$ . By comparison, setups with only  $\sim 1.4 \text{ mM}$  dissolved monomeric silica present initially showed no silica precipitation independent of the temperature and the concentration remained constant for the duration of the experiment.

The second experiment, which was designed to test the influence of Fe(II), cells and light on amorphous silica precipitation during the cold period (Fig. 3, panel B), showed an initial strong decrease of  $\text{Fe}^{2+}$  after the removal of  $\text{Fe}^{2+}$ -containing medium and the addition of neutralized monomeric silica from approximately  $4.9 \text{ mM Fe}^{2+}$  to  $3.9 \text{ mM Fe}^{2+}$ . Over the course of the experiment the  $\text{Fe}^{2+}$  concentration further decreased to approximately  $3.5 \text{ mM}$ . Nonetheless, no visible formation of Fe(III) (oxyhydr)oxides was observed. The  $\text{Fe}^{2+}$  concentration in the abiotic control stayed constant after the initial decrease. The dissolved monomeric silica concentration showed a strong decrease after the first 48 h and remained constant for the remainder of the experiment.

Additionally, we determined the influence of low temperatures ( $5^\circ\text{C}$ ) on the ability of *R. iodosum* to oxidize Fe(II) and whether the formation of Fe(III) (oxyhydr)oxides would be expected under these conditions. Therefore, the temperature was kept constant at  $5^\circ\text{C}$  while keeping the vials illuminated (Fig. 4, panel A). The biotic triplicates showed a slight decrease in  $\text{Fe}^{2+}$  from an initial concentration of approximately  $4.9 \text{ mM}$  to  $4.2 \text{ mM}$  at the end of the experiment. However, no visible orange-colored Fe(III) (oxyhydr)oxides were observed. The  $\text{Fe}^{2+}$  concentration in the abiotic (non-inoculated) control decreased slightly from an initial concentration of approximately  $5 \text{ mM}$  to a final concentration of approximately  $4.7 \text{ mM}$ . The Fe(II) oxidation rates of the biotic triplicates and the abiotic control showed only a minor deviation with  $0.03 \text{ mM d}^{-1}$  and  $0.02 \text{ mM d}^{-1}$ , respectively. The dissolved monomeric silica concentration remained constant over the course of the experiment for both the biotic triplicates and the abiotic (non-inoculated) abiotic control.

During the second warm period of the main experiment (days 133–168, Fig. 2), *R. iodosum* oxidized approximately  $0.9 \text{ mM}$  of  $\text{Fe}^{2+}$  in the biotic setups within 4 to 7 days, yielding maximum oxidation rates of ca.  $0.2 \text{ mM d}^{-1}$  (Fig. 2). Fe(II) oxidation is also indicated by the precipitation of orange-colored Fe(III) minerals on top of the amorphous silica layer (Fig. 1C). The removal of  $\text{Fe}^{2+}$  from solution was  $>92\%$ . In contrast to the first warm period, the monomeric silica concentrations during the second warm period remained at amorphous silica saturation ( $2.2 \text{ mM}$ ). These values are approximately 35% higher than the initial monomeric silica concentration at the beginning of the experiment and almost 24% higher than corresponding average values during the cold period. It thus appears that the amount of monomeric silica removed during Fe(II) oxidation is affected by the amount of  $\text{Fe}^{2+}$  oxidized, and as expected, the remaining concentration of monomeric silica is influenced by the high and low temperatures. At the same time the remaining dissolved  $\text{Fe}^{2+}$  concentration in the

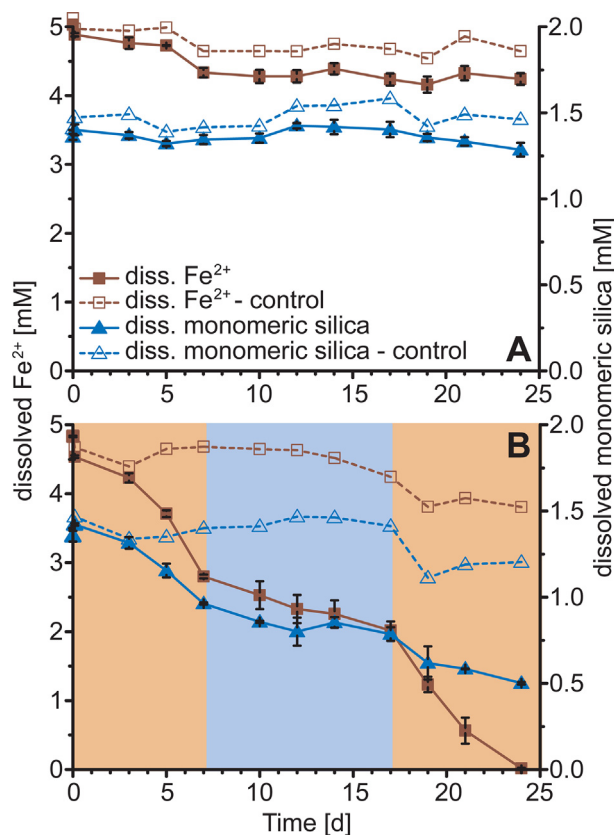


Fig. 4. Development of dissolved  $\text{Fe}^{2+}$  and monomeric silica concentrations over time for: (A) incubation of *R. iodosum* at  $5^\circ\text{C}$  and light, and (B) incubation of *R. iodosum* under changing temperature conditions and light. Data for biotic setups are the mean from triplicates  $\pm$  standard deviation while the data for the abiotic (non-inoculated) controls represent single measurements. Orange shaded areas in panel (B) represent incubation at  $26^\circ\text{C}$ , while blue shaded areas mark incubation at  $5^\circ\text{C}$ . (For interpretation of the references to color in this figure legend, the reader is referred to the web version of this article.)

abiotic setup increased consistently from  $1.9 \text{ mM}$  on day 133 to  $2.8 \text{ mM}$  at the end of the experiment. The abiotic setup showed similar trends in monomeric silica concentrations as the biotic setups, i.e., changing silica solubility at low vs. high temperatures controls silica precipitation and thus the remaining silica concentrations in solution.

Crucial to the temperature cycling model envisioned in our study is the ability of *R. iodosum* to recover and resume Fe(II) oxidation after a prolonged phase of cold temperatures. Therefore, we performed an additional experiment under varying temperature conditions to verify the ability of *R. iodosum* to resume Fe(II) oxidation after inactivity during a cold period (Fig. 4, panel B). *R. iodosum* showed rapid initial Fe(II) oxidation with rates of  $0.36 \pm 0.02 \text{ mM d}^{-1}$ , rates similar to the main experiment (Fig. 2, day 0–13), and formation of orange-colored Fe(III) (oxyhydr)oxides during the first warm period (Fig. 4B,  $26^\circ\text{C}$ , day 0–7). During the following cold period (Fig. 4B,  $5^\circ\text{C}$ , day 7–17) the Fe(II) oxidation rate decreased

to  $0.07 \pm 0.01 \text{ mM d}^{-1}$ , resulting in a decrease of the  $\text{Fe}^{2+}$  concentration from approximately 2.8–2.0 mM. The increase in temperature to 26 °C during the second warm period (Fig. 4B, day 17–24) resulted in *R. iodosum* oxidizing Fe(II) at rates comparable to the first warm period ( $0.36 \pm 0.04 \text{ mM d}^{-1}$ ), showing that *R. iodosum* would theoretically be able to recover from prolonged cold stress. During the first warm period, approximately 32% of the initially present dissolved monomeric silica was removed from solution. During the following cold period and the second warm period another 18% and 15% dissolved monomeric silica, respectively, were removed from solution. The  $\text{Fe}^{2+}$  and dissolved monomeric silica concentrations of the abiotic (non-inoculated) control remained relatively constant until the end of the experiment.

### 3.3. Properties of Fe(III) mineral precipitates

To identify the mechanism which led to the separate precipitation of Fe- and Si-rich minerals, we analyzed the mineral identity, structure and morphology, as well as the charge ( $\zeta$ -potential) of the primary minerals formed either by *R. iodosum* or by abiotic reaction of  $\text{Fe}^{2+}$  with  $\text{O}_2$ . The X-ray diffractograms of the precipitates formed in the presence of *R. iodosum*, both in the absence as well as in the presence of dissolved silica, showed reflections representative for NaCl, stemming from the salt-rich marine medium (Fig. 5A). The sample taken from Fe(III) mineral precipitates formed in the absence of silica showed additional reflections representative of goethite, where the broad base, relatively low intensity and signal quality suggest goethite being present in a low crystalline form. The Fe(III) mineral precipitates formed in the presence of silica showed no additional reflections and were X-ray amorphous with regard to the Fe-bearing mineralogy.

Both biogenic Fe(III) minerals formed by *R. iodosum* in the absence or presence of silica were additionally identified by Moessbauer spectroscopy. For the minerals precipitated in the absence of silica, two distinct mineral phases were identified in the Moessbauer spectrum measured at 77 K (Fig. 5B). A mineral phase identified as biogenic ferrihydrite by its paramagnetic doublet and fitting parameters (Table 1; Eickhoff et al., 2014) made up for 52.5% of all minerals present. The second mineral phase, which made up 47.5% of the fit, was most closely related to goethite and identified by its parameters (Table 1) as well as its partial magnetic ordering and collapsed sextet (Halama et al., 2016). This interpretation was supported by Moessbauer spectra obtained at 5 K (Appendix A, Fig. A.1). The biogenic minerals precipitated in the presence of silica (Fig. 5C) consisted mainly of ferrihydrite (90.8%), which was identified by its paramagnetic doublet, an isomer shift of  $0.46 \text{ mm s}^{-1}$  and a quadrupole shift of  $0.80 \text{ mm s}^{-1}$  in the spectrum measured at 77 K (Eickhoff et al., 2014; Halama et al., 2016). A second, hitherto unidentified Fe(III) phase comprised 9.2% of the fitting (Table 1). However, this second mineral phase was not found in Moessbauer spectra obtained at 5 K. Here, biogenic ferrihydrite made up for 100% of the fit and was identified by its parameters (Appendix A, Table A.2).

Based on SEM analyses, cell-Fe(III) mineral aggregates precipitated in the absence of silica generally showed close association between cells and minerals (Fig. 5D). Aggregate sizes were  $7.6 \pm 5.2 \text{ }\mu\text{m}$  as determined by electron microscopy. The surface of the minerals was rough and needle-like, forming bulb-like structures. Compared to the biogenic cell-Fe(III) mineral aggregates precipitated in the absence of silica, the biogenic aggregates formed in the presence of silica showed less cells associated with the minerals. Furthermore, the minerals formed by bacteria in the presence of silica were smooth and appeared to consist of bulb-like shapes that stuck together (Fig. 5E). Their average size was  $10.3 \pm 9.3 \text{ }\mu\text{m}$ . However, in both cases, despite being associated with the Fe(III) minerals, the cells generally seemed to be free of mineral precipitates. Calculated settling velocities, based on a density of  $2 \text{ g cm}^{-3}$  (Posth et al., 2010), for aggregates formed in the absence of silica were  $0.56 \text{ m h}^{-1}$  and  $1.03 \text{ m h}^{-1}$  for aggregates formed in the presence of silica. However, it must be pointed out that using SEM (a 2D technique) for aggregate size analysis likely introduced a size analysis bias into our measurements in that the aggregate sizes reported above likely differ from the true aggregate sizes. Consequently, the settling velocities calculated above would also either be faster or slower, resulting in uncertainty regarding the water column residence time of the aggregates.

Abiotic aggregates precipitated by  $\text{O}_2$  in the absence of silica showed a similar mineral shape and morphology as their biogenic equivalents but with individual aggregates being more intertwined and linked to each other (Fig. 5F). The average size of the abiogenic Fe(III) mineral aggregates was  $8.6 \pm 7.6 \text{ }\mu\text{m}$ . The abiogenic Fe(III) mineral aggregates precipitated in the presence of silica appeared to be the smallest of all aggregates investigated (Fig. 5G). However, the individual small aggregates were so intertwined and associated with each other that individual aggregate sizes could not be accurately measured.

To determine whether cells or cell debris co-precipitated with the Fe(III) minerals might influence the surface charge of the minerals, thus preventing the silica from becoming sorbed, we performed  $\zeta$ -potential measurements (with samples diluted 1:10 with 10 mM HEPES-buffered MilliQ® water). The measurements showed that the surface charge for biogenic Fe(III) mineral-cell aggregates produced by *R. iodosum* was very negative with  $-23.5 \pm 1.4 \text{ mV}$ , while the abiotically precipitated Fe(III) minerals showed much less negative values of  $-16.3 \pm 0.7 \text{ mV}$  (Fig. 6A). This suggests that in blank water containing HEPES buffer the biogenic Fe(III) minerals are expected to be less likely to bind negatively charged silica than the abiogenic Fe(III) minerals.

In order to apply particle reactivity in terms of BIF, it is further important to determine the particle surface charge under relevant ancient ocean marine conditions. When taking this into account, we found that for an increasing ratio of marine medium to MilliQ® water, the  $\zeta$ -potential of 2-line ferrihydrite (corresponding to the abiogenic Fe(III) minerals) increased from  $-12.5 \pm 2.6 \text{ mV}$  for MilliQ® water to only  $-3.7 \pm 0.4 \text{ mV}$  (1:1 ratio medium to MilliQ® water) and to  $-1.7 \pm 3.4 \text{ mV}$  for medium only (Fig. 6B).

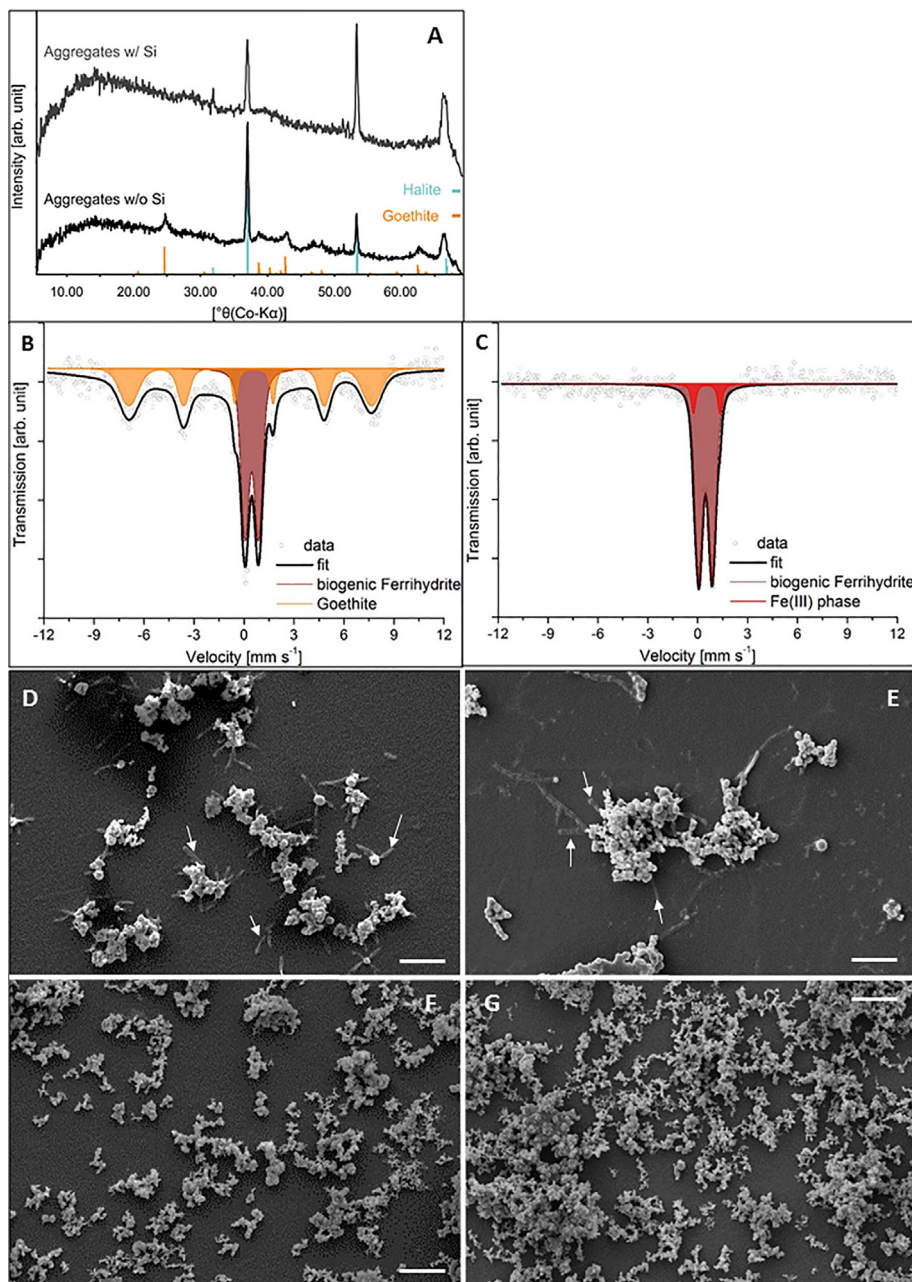


Fig. 5. Identity and structure of biogenic and abiogenic Fe(III) mineral precipitates. (A) shows X-ray diffractograms of Fe(III) minerals formed by *R. iodosum* in the presence and absence of silica. (B) and (C) show Mössbauer spectra collected at 77 K (data for 5 K measurements is shown in the supporting information). Circles represent collected data points while the solid black lines represent the fit. (B/C) represent spectra collected from Fe(III) minerals precipitated by *R. iodosum* in the absence of silica (B) and presence of silica (C). (D-G) SEM micrographs taken from Fe(III) minerals either precipitated by *R. iodosum* in the absence of silica (D), Fe(III) minerals precipitated by *R. iodosum* in the presence of silica (E), abiogenic Fe(III) minerals precipitated by addition of  $\text{O}_2$  to silica-free medium (F), and abiogenic Fe(III) minerals precipitated by addition of  $\text{O}_2$  to silica-containing medium (G). The size bar in all SEM micrographs is 5  $\mu\text{m}$ . Cells are indicated by white arrows.

These results clearly suggest that under marine water (ancient ocean) conditions, the abiogenic Fe(III) minerals are almost neutrally charged and are expected to bind the negatively charged silica ions to a large extent. This is in contrast to the biogenic Fe(III) minerals formed by *R. iodosum* where the average  $\zeta$ -potential value

$-27.4 \pm 1.4$  mV in MilliQ<sup>®</sup> water increased to  $-21.3 \pm 1.6$  mV for a 1:1 ratio mixture of MilliQ<sup>®</sup> water to medium and to  $-17.8 \pm 2.0$  mV for medium only (Fig. 6B). This shows that even when the geochemical composition of the seawater is considered, the biogenic cell-Fe(III) mineral aggregates remain negatively charged in contrast to the

Table 1

Moessbauer spectroscopy data obtained at 77 K for biogenic Fe(III) minerals precipitated by *R. iodosum* in the presence or absence of silica. <sup>1</sup>IS = isomer shift, <sup>2</sup>QS = quadrupole shift, <sup>3</sup>B<sub>hf</sub> = hyperfine field, <sup>4</sup>Fh = ferrihydrite.

	IS <sup>1</sup> [mm s <sup>-1</sup> ]	QS <sup>2</sup> [mm s <sup>-1</sup> ]	B <sub>hf</sub> <sup>3</sup> [T]	Area [%]
<b>No silica</b>				
Biog. Fh <sup>4</sup>	0.46	0.81	–	52.5
Goethite	0.48	–0.11	45.19	47.5
<b>With silica</b>				
Biogenic Fh <sup>4</sup>	0.46	0.80	–	90.8
Fe(III) phase	0.53	1.58	–	9.2

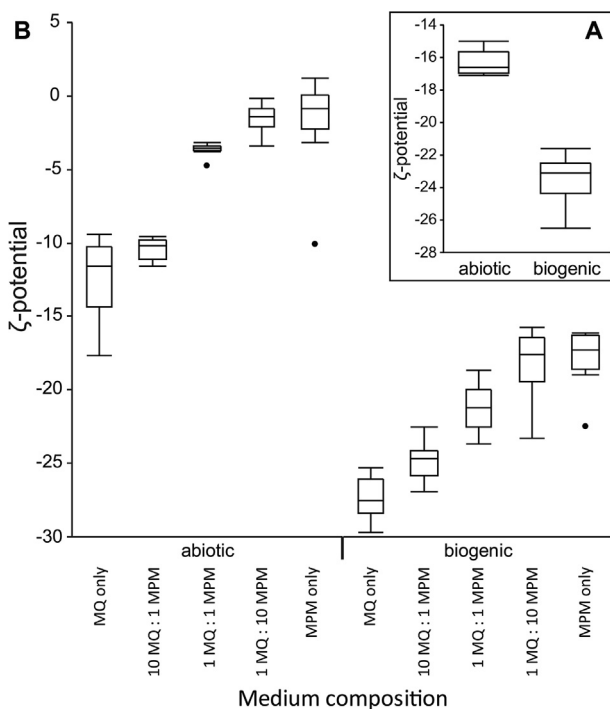


Fig. 6. Surface charge of Fe(III) minerals given as  $\zeta$ -potential. All measurements represent replicate measurements where  $n = 9$ . The insert (A) shows the  $\zeta$ -potential of abiotic Fe(III) minerals compared to biogenic Fe(III) minerals formed by *R. iodosum* obtained in pure MilliQ<sup>®</sup> water (MQ). The large plot (B) shows the  $\zeta$ -potential of 2-line ferrihydrite compared to biogenic Fe(III) minerals formed by *R. iodosum* depending on the geochemical composition of the medium, ranging from pure MilliQ<sup>®</sup> water (MQ), different water-medium mixtures, to pure marine phototroph medium (MPM).

abiotic Fe(III) minerals, resulting in an expected repulsion of silica (or at least binding to a much lesser extent) and thus potentially allowing the formation of alternating Fe- and Si-rich mineral layers.

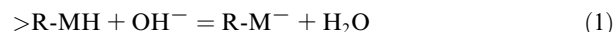
### 3.4. Surface reactivity of the cell-mineral aggregates

Potentiometric titrations were performed in conjunction with FITEQL modeling to determine the  $pK_a$  and site con-

centrations of surface active functional groups for the *R. iodosum* Fe(III) mineral-cell aggregates. Protonation models invoking 2–4 sites were tested in FITEQL, with a model employing two proton active surface functional sites providing the only converging fit in FITEQL. The site  $pK_a$  and site concentration per gram of Fe(III) mineral-cell aggregate are presented in Table 2, with the values for site 1 being 3.35 and  $4.96 \times 10^{-5}$ , respectively; while site 2 had a  $pK_a$  value of 8.50 and a site concentration per gram of  $1.42 \times 10^{-4}$ , over twice as abundant as site 1. Site 1 likely corresponds to carboxyl/phosphodiester groups, whereas site 2 corresponds to amino groups.

Fig. 7 shows the titration data for  $2.5 \text{ g L}^{-1}$  Fe(III) mineral-cell aggregate plotted in terms of the difference in mol added of 0.1 M HCl and 0.1 M NaOH per gram of Fe(III) mineral-cell aggregates. The slope of the titration curve at any point gives the instantaneous buffering capacity of the Fe(III) mineral-cell aggregates, corresponding to the rate of deprotonation of its surface. The areas with the greatest slope correspond to the regions where buffering capacity of each site is highest, which correlates with the functional group  $pK_a$  values.

The titration data demonstrate that the Fe(III) mineral-cell aggregates have a high buffering capacity between each of the two  $pK_a$  values, where a large addition of titrant produces a comparably minor change in pH. Minimal hysteresis was observed between the “up” and “down” titrations, further indicating limited dissolution and cell damage between titrations, and that the protonation/deprotonation of the cell wall functional groups were reversible. The mass action equation for the deprotonation of the generalized surface functional group is given by:



where M represents the surface functional group attached to the surface ( $>R$ ) of the Fe(III) mineral-cell aggregate. As shown by Eq. (1), the addition  $OH^-$  (i.e. increasing pH) causes deprotonation of the surface ligands, leaving them with a negative surface charge. As pH increases, the surface of the Fe(III) mineral-cell aggregates becomes progressively deprotonated, causing a net negative surface charge. This is corroborated by the  $\zeta$ -potential measurements which show a highly negative surface charge for the biogenic Fe(III) mineral-cell aggregates.

### 3.5. Mineral saturation states

In order to determine silica speciation and the saturation states of the different silica minerals and Fe(II)-silicates at different temperatures, we performed geochemical modelling based on the composition of the marine phototroph medium and the Fe(II) and monomeric silica present in the experiments.

The results of the geochemical modelling (Table 3) showed that no formation of greenalite is expected under the experimental conditions. However, both a decrease in temperature from 26 °C to 5 °C or an increase in the monomeric silica concentration (as during the cold period or in experiments with silica oversaturation) increased the potential for greenalite formation. For the initial medium

Table 2

pK<sub>a</sub> and site concentration per gram of Fe(III) mineral-cell aggregates for replicate measurements displayed as mean from triplicates ± standard deviation. A 2-site FITEQL model was employed to fit the titration data. <sup>1</sup>Assignment of functional groups is tentative and based on references (Cox et al., 1999; Sokolov et al., 2001; Martinez et al., 2002; Liu et al., 2015).

Surface site	Mean pK <sub>a</sub>	Site concentration [10 <sup>-4</sup> mol g <sup>-1</sup> aggregates]	Suggested functional group <sup>1</sup>
1	3.35 ± 0.49	0.50 ± 0.01	carboxyl/phosphodiester
2	8.50 ± 0.02	1.42 ± 0.22	amino

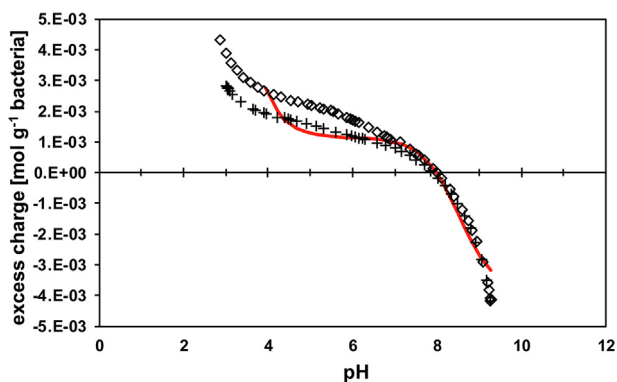


Fig. 7. Titration curve for Fe(III) mineral-cell aggregates plotted in terms of mol of base subtracted from mol of acid added per gram of bacteria (excess charge) for the pH 3 to 9 and 9 to 3 titrations. Crosses represent the forward (pH 3–9) titration while open diamonds represent the reverse (pH 9–3) titration. The FITEQL model is plotted in red with the inflection points being the pK<sub>a</sub> values. (For interpretation of the references to color in this figure legend, the reader is referred to the web version of this article.)

composition (3.5 mM Fe<sup>2+</sup> and ~1.4 mM dissolved monomeric silica) a temperature decrease from 26 °C to 5 °C resulted in a change from a slight undersaturation with respect to amorphous silica to a slight oversaturation with respect to amorphous silica. In experiments with a high degree of silica oversaturation (cold phase precipitation experiment and silica precipitation kinetic experiment), the formation of amorphous silica was generally expected when a decrease in temperature lowered the solubility of amorphous silica. The model generally predicted the presence of cristobalite and quartz on the basis of their lower solubility and higher thermodynamic stability, however, in reality both crystallize from an amorphous silica precursor through dissolution-reprecipitation reactions (Williams et al., 1985). The major dissolved silica species in all simulations was H<sub>4</sub>SiO<sub>4</sub> and generally accounted for >99%.

Table 3

Summary of saturation indices (SI) calculated with Visual MINTEQ vs. 3.1 for the initial marine phototroph medium (medium) and Si oversaturation experiments, based on pH, geochemical composition of the medium and temperature.

Mineral	Initial medium		Si oversaturation (8 mM)	
	SI, 26 °C	SI, 5 °C	SI, 26 °C	SI, 5 °C
Greenalite	-2.16	-2.02	-0.64	-0.51
SiO <sub>2</sub> (am, gel)	-0.09	0.09	0.67	0.85
SiO <sub>2</sub> (am, ppt)	-0.06	0.14	0.70	0.90
Cristobalite	0.55	0.81	0.55	1.57
Quartz	1.19	1.50	1.95	2.25

## 4. DISCUSSION

### 4.1. Fe(II) oxidation by *R. iodosum* in the presence of Si and mineral (trans)formation

Several studies have suggested an important role of phototrophic Fe(II)-oxidizing bacteria (photoferrotrophs) during the deposition of Archean BIF and emphasized their potential role in the formation of these ancient sedimentary deposits (Widdel et al., 1993; Ehrenreich and Widdel, 1994; Konhauser et al., 2002; Kappler et al., 2005; Li et al., 2011; Jones et al., 2015). Analysis of the BIF rock record even suggests their activity as early as ca. 3.8 Ga (Mloszewski et al., 2012; Czaja et al., 2013; Martinez et al., 2016). While we appreciate that microaerophilic Fe(II)-oxidizing bacteria could have contributed to BIF deposition once there was sufficient oxygen available to fuel their metabolism (Holm, 1987; Konhauser et al., 2002; Smith et al., 2013; Chan et al., 2016), for the scope of our study we specifically envision an Archean ocean devoid of oxygen.

In order to investigate the alternating deposition of Fe- and Si-rich mineral layers and to simulate an Archean ocean environment with elevated Fe<sup>2+</sup> (Poulton and Canfield, 2011) and silica concentrations (Maliva et al., 2005), we grew *R. iodosum* in a marine medium starting with 3.5 mM Fe<sup>2+</sup> and 1.4 mM monomeric silica during warm and cold periods. Additionally, during the cold period of the main experiment and selected control experiments (see Figs. 2 and 3), 8 mM dissolved monomeric silica were added. *R. iodosum* showed maximum oxidation rates of up to 0.6 mM d<sup>-1</sup> during the first warm period and maximum rates of 0.2 mM d<sup>-1</sup> during the second warm period. No obvious lag phase was observed in both cases. In fact, during the first warm period 28% of the initial Fe<sup>2+</sup> was already oxidized within 6 days, while during the second warm period 42% of the initially present Fe<sup>2+</sup> was oxidized within 3 days. This is in contrast to previous work which observed a lag phase of 7–9 days for the same strain (Straub et al., 1999; Wu et al., 2014). A potential explana-

tion for this observation is that pre-cultivation, and therefore, a high degree of adaptation of our strain, occurred prior to our experiments, resulting in a lack of an obvious lag phase in the experiments. Our data also suggests that the presence of ca. 1.4 mM monomeric silica does not negatively influence Fe(II) oxidation, which is in line with observations from previous studies (Posth et al., 2008; Wu et al., 2014; Gauger et al., 2016). Gauger et al. (2016) and Wu et al. (2017) also showed that the presence of dissolved monomeric silica actually increased Fe(II) oxidation rates, potentially by reducing toxicity effects related to high Fe<sup>2+</sup> concentrations in the presence of light (Bird et al., 2013; Swanner et al., 2015a). The maximum oxidation rate determined for the first warm period (Fig. 2) correlates well with the results of other studies where photoferrotrophs were grown in silica-containing medium. They found comparable oxidation rates for other marine photoferrotrophs (Swanner et al., 2015b; Laufer et al., 2017) or freshwater photoferrotrophs grown in Si-rich conditions with comparable Fe<sup>2+</sup> concentrations (Konhauser et al., 2007). The maximum oxidation rates of 0.2 mM d<sup>-1</sup> derived for the second warm period are comparable to results of Wu et al. (2014) who reported rates of 0.25 mM d<sup>-1</sup> for Fe<sup>2+</sup> concentrations of 0.7 mM.

Overall the oxidation rates determined in our study agree well with previous results and suggest that photoferrotrophs could have been active under the high Fe and silica conditions relevant for an Archean ocean. Although those previous studies, and our work here as well, showed that oxidation rates of photoferrotrophs depend on the initial Fe(II) concentration (Hegler et al., 2008; Wu et al., 2014), the experimental data presented here add to an increasing pool of indirect evidence which suggests that photoferrotrophs could have been active in an Archean ocean and could have facilitated the deposition of BIFs.

The validity of the temperature-dependent model for the alternating precipitation of Fe and silica layers in BIFs envisioned in the present study additionally depends on a predicted low activity of photoferrotrophs at low temperatures. Although the individual influence of Fe<sup>2+</sup> concentration, light intensity and temperature on photoferrotrophic Fe(II) oxidation rates have been investigated in the past (e.g. Hegler et al., 2008; Posth et al., 2008; Wu et al., 2014), no study exists that investigated the combination of these factors. In this regard, our study provides a first step to resolve this knowledge gap by showing that the model strain *R. iodotum* was significantly less active at low temperatures. By extension these results suggest that photoferrotrophs should essentially be inactive if not only the temperature is lowered but especially and even more under low Fe(II) conditions, thereby allowing a separate deposition of Si-rich layers in BIFs.

There is considerable agreement that the precursor minerals to BIFs were likely poorly crystalline or amorphous Fe(III) (oxyhydr)oxides (Konhauser et al., 2002; Kappler et al., 2005; Klein, 2005; Posth et al., 2014; Sun et al., 2015; Robbins et al., 2019) or a silica-containing ferrihydrite (Percak-Dennett et al., 2011; Alibert, 2016; Zheng et al., 2016). The mineralogical data obtained in this study provide support for this claim as a poorly crystalline, X-ray

amorphous Fe(III) phase, most likely ferrihydrite, as well as fine-grained goethite were found. This is principally in line with previous studies with *R. iodotum* (Wu et al., 2014; Swanner et al., 2015b; Wu et al., 2017), although we found no lepidocrocite, which could potentially be attributed to the higher bicarbonate (HCO<sub>3</sub><sup>-</sup>) concentration used in the present study, promoting the formation of goethite over lepidocrocite (Larese-Casanova et al., 2010). Additionally, the Fe mineralogy showed a clear dependence on the presence or absence of silica. While a mixture of ferrihydrite and goethite was formed in the medium containing no silica, the presence of silica clearly prevented the formation of more crystalline mineral phases, resulting in the formation of ferrihydrite only. This effect has been observed in the past (Cornell et al., 1987; Jones et al., 2009; Toner et al., 2012; Eickhoff et al., 2014) and is probably related to silica blocking sorption sites for Fe(II), thereby preventing Fe(II)-catalyzed transformation of ferrihydrite into thermodynamically more stable minerals like goethite (Posth et al., 2014).

The constant settling of primary Fe(III) (oxyhydr)oxides produced by photoferrotrophs through the water column could have been subjected to further secondary mineral transformations, e.g., reaction with Fe<sup>2+</sup> sourced from hydrothermal vent sites and transported to the shelf regions were BIFs were deposited. The reaction between primary Fe(III) (oxyhydr)oxides and Fe<sup>2+</sup> could have resulted in the formation of meta-stable green rust and perhaps the formation of nanosized magnetite as secondary minerals (Li et al., 2017; Koeksoy et al., 2019). Alternatively, Fe(III)-reducing bacteria could have used the co-precipitated organic carbon to (partially) reduce the primary Fe(III) minerals forming secondary Fe(II)-bearing minerals such as magnetite. Such a mechanism was initially proposed by Walker (1984) and independently confirmed by experimental studies and C and Fe isotope analysis of the BIF rock record (e.g. Heimann et al., 2010; Steinhöfel et al., 2010; Craddock and Dauphas, 2011; Li et al., 2013). However, recent work has shown that a close association of ferrihydrite and organic matter may inhibit Fe atom exchange between Fe(II) and ferrihydrite (Thomas-Arrigo et al., 2017), thus preventing the formation of more crystalline mineral phases during the abiotic reaction of ferrihydrite-organic matter coprecipitates with Fe(II) (Thomas-Arrigo et al., 2018; Zhou et al., 2018). Consequently, organic matter coprecipitated with biogenic Fe(III) minerals could have prevented the secondary transformation of minerals such as magnetite. Indeed, the minerals formed were generally closely associated with bacterial cells, forming cell-Fe(III)-mineral aggregates. Nevertheless, many of the cells remained free of encrustation, which appears to be a common feature for photoferrotrophs (Kappler and Newman, 2004; Schaedler et al., 2009; Posth et al., 2010; Wu et al., 2014; Gauger et al., 2015; Gauger et al., 2016; Laufer et al., 2017).

Results from this study and others demonstrate that different strains associate with Fe(III) minerals to different extents, and in some cases become partially encrusted. For example, in a study by Kappler and Newman (2004) the freshwater photoferrotroph *R. ferrooxidans* strain

SW2 showed partial association of minerals with cells during the initial growth phase but none after several months of incubation. Laufer et al. (2017) reported a close association between cells of a marine photoferrotroph and Fe(III) minerals where the cells remained free of any mineral encrustation, which is comparable to results by Wu et al. (2014) with the marine photoferrotroph *R. iodosum*. Other studies with photoferrotrophs showed that cells were only loosely attached to Fe(III) minerals or not associated at all (Hegler et al., 2008; Schaedler et al., 2009). This has implications for the use of different bacterial strains as model strains for BIF deposition. Depending on the extent to which cells and Fe(III) minerals are co-precipitated, different C:Fe ratios in the settling aggregates and the sediments will be obtained. Consequently, depending on the strain which is being used in different studies, contradicting conclusions might be drawn on the importance of biomass for the trace element budget (Konhauser et al., 2017b), co-precipitation and sorption of trace elements to biogenic Fe(III) (oxyhydr)oxides (e.g. Eickhoff et al., 2014) or post-depositional and (early) diagenetic (microbial) processes (Posth et al., 2013; Posth et al., 2014; Halama et al., 2016). Moreover, the characteristics of the aggregates formed not only depend on whole cells co-precipitated with the Fe(III) minerals but also on cell debris and organic molecules which are either released upon cell death or actively excreted by living cells. For example, *R. iodosum* has been shown in previous studies to form EPS (Wu et al., 2014). Therefore, it seems conceivable that a mixture of those organic compounds and cells might influence the characteristics of the minerals and in particular the mineral surface in a way which leads to the separate deposition of Fe(III) minerals and silica.

#### 4.2. Abiotic silica mineral saturation, precipitation and formation of silica layers in BIF

The Archean ocean was not only ferruginous but also rich in silica, with concentrations of up to 2.2 mM (saturation with respect to amorphous silica; Maliva et al., 2005); this is reflected in the high silica content of BIFs - up to 50 wt.% SiO<sub>2</sub> (Trendall, 2002). According to the model initially suggested by Posth et al. (2008), the precipitation of the Si-rich layers in BIFs was triggered by a decrease in temperature causing supersaturation with regards to amorphous silica. We therefore simulated the precipitation of amorphous silica under conditions relevant for the Archean ocean triggered by a decrease in temperature and performed complementary experiments where we determined silica precipitation kinetics and the influence of the presence of *R. iodosum*, Fe<sup>2+</sup> and light on the formation of these silica layers.

We also used geochemical modelling to assess whether our experimental conditions with Fe<sup>2+</sup> and silica led to the formation of amorphous silica or Fe-silicates such as greenalite (e.g. Rasmussen et al., 2013; Rasmussen et al., 2015; Tosca et al., 2016; Rasmussen et al., 2017; Johnson et al., 2018). Our modelling results suggested that under the given geochemical conditions no greenalite formation is to be expected, independent of the temperature, and

amorphous silica should be the dominant silica species being formed. However, in contrast to our experimental results, the geochemical modeling showed that there was a temperature dependence for amorphous silica formation at 1.4 mM where at higher temperatures (26 °C) the solution was undersaturated with regards to amorphous silica and only at lower temperatures (5 °C) did silica precipitate, as expected based on Gunnarsson and Arnórsson (2000).

Another factor which could potentially influence the formation of the initial amorphous silica layers is the activity of photoferrotrophs at low temperatures which could lead to the coprecipitation of some Fe(III) (oxyhydr)oxides with the amorphous silica. Based on our experimental results, only minor activity of photoferrotrophs during cold periods is expected. Additionally, although minor Fe(II) oxidation occurred in silica precipitation experiments with *R. iodosum*, Fe<sup>2+</sup> and light at low temperature, no Fe(III) (oxyhydr)oxides were detected, suggesting the formation of almost pure amorphous silica layers.

One critical point about our experiments is that a certain degree of oversaturation with regards to amorphous silica (8 mM dissolved monomeric silica, approximately 4× the saturation of amorphous silica) was necessary to achieve silica precipitation and the formation of an amorphous silica layer. Consequently, it seems likely that the silica precipitated as a result of this oversaturation instead of the temperature change, as suggested by our abiotic silica precipitation experiments (Fig. 3) and the results of our geochemical modelling (Table 3). One potential reason for this lack of silica precipitation after several weeks in the experiments to create alternating layers of Fe(III) minerals and amorphous silica (Figs. 1 and 2) could be a lack of nucleation sites that are necessary to initiate the silica precipitation, resulting in a much higher silica concentration needed for the formation of an amorphous silica layer. Theoretically, the already present cell-Fe(III) mineral aggregates deposited at the bottom of the vials could have served as nucleation for silica precipitation. However, based on visual inspection, the presence of those cell-Fe(III) mineral aggregates did not seem to have induced any silica nucleation. One potential reason could be the presence of organic matter produced by the bacteria, which would have prevented the initial sorption of silica onto the Fe(III) minerals (as lined out below in Section 4.3). Another potential reason for the absence of silica precipitation could be that the formation of silica gels at neutral pH is very slow (Krauskopf, 1956 and references therein). Moreover, silicification takes place in three discrete steps (Iler, 1979) where silica polymers are first formed (explaining the fast decline in dissolved monomeric silica concentration), these polymers then slowly increase in size until the polymers grow into chains and networks, and finally they form a visible amorphous silica gel. However, these results are at odds with the silica precipitation control experiments, where we observed the same rapid decline in dissolved monomeric silica (Fig. 3), but a visible amorphous silica layer formed already after 3–5 days. Currently we have no explanation for this discrepancy. In addition, our silica precipitation control experiments showed that the decrease in temperature from 26 °C to 5 °C, while slightly accelerating

the removal of monomeric silica from solution, had no further effect on silica precipitation (Fig. 3). Instead, rather than influencing the initial silica precipitation kinetics, lowering the temperature from 26 °C to 5 °C resulted in a significant decrease in the equilibrium concentration of dissolved monomeric silica at 5 °C compared to 26 °C ( $1.47 \pm 0.04$  mM and  $1.89 \pm 0.03$  mM, respectively; Fig. 3). This suggests that in order to precipitate amorphous silica from solution oversaturation was required in our experiments. In summary, while temperature certainly modulated the activity of photoferrotrophs and therefore Fe(III) mineral precipitation, based on our experiments silica precipitation required (in addition to lower temperatures) either a high degree of oversaturation or the presence of nucleation sites, such as bacterial cells, to precipitate amorphous silica layers.

In order to create an amorphous silica layer, we envision a model (as in Fig. 8) where during the warm period (spring and summer), while the photoferrotrophs are active, the silica reservoir increases. With the onset of autumn, the photoferrotrophs become less active due to lower temperatures and silica starts to precipitate. In winter significant silica precipitation takes place leading to the formation of Si-rich layers, while the photoferrotrophs are mostly inactive and the  $\text{Fe}^{2+}$  reservoir replenishes. Once the equilibrium concentration at low temperatures is reached, no further sil-

ica precipitation takes place. With the increase in temperature in the spring the photoferrotrophs resume their metabolic activity resulting in the onset of Fe(III) mineral precipitation and formation of the next Fe-rich layer while the dissolved monomeric silica reservoir replenishes during the warm period.

#### 4.3. Mechanism responsible for separated deposition of Fe- and Si-rich layers in BIFs

The previous study by Posth et al. (2008), and the results of the present study, suggest minor co-precipitation of silica and Fe(III) minerals. This implies that temperature might have acted as the unifying trigger for the alternating deposition of Si- and Fe-rich layers in BIFs. However, in addition to temperature, another factor must be responsible for the reduced silica binding to the Fe(III) minerals, as the absence of silica-Fe-co-precipitation (as previously reported by Percak-Dennett et al., 2011; Zheng et al., 2016), and the independent precipitation of Fe-rich and Si-rich layers initially remained unclear. Based on our experimental results we suggest that organic molecules, cell debris, and whole cells which were co-precipitated with the Fe(III) minerals led to changes in the mineral surface properties, minimizing sorption of silica to the Fe(III) minerals, thus preventing co-precipitation of silica. To identify the

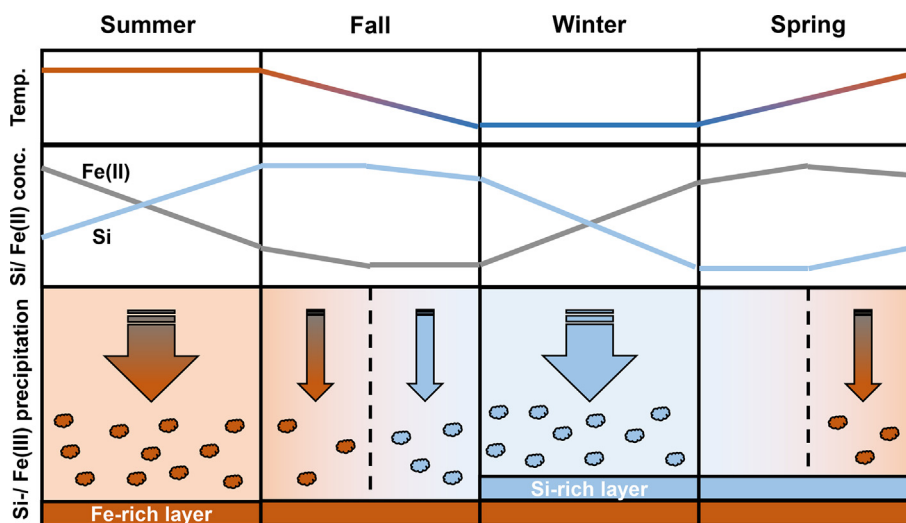


Fig. 8. Course of Fe and silica precipitation depending on temperature. Orange colors indicate high temperatures and Fe(III) precipitation, blue colors correspond to cold temperatures and silica precipitation; grey color shows dissolved Fe(II) concentration. Arrows pointing downwards represent Fe(III) or silica precipitation. The thickness of the arrows represents the extent of Fe(III) or silica precipitation. During **summer** there is extensive Fe(III) mineral precipitation due to the activity of photoferrotrophs, leading to the formation of Fe(III)-rich layers and depletion of the Fe(II) reservoir. At the same time, due to higher solubility at higher temperatures and due to riverine and/or hydrothermal input, the silica reservoir is increased during summer. As the temperature starts to decrease in **autumn**, the photoferrotrophs become less active, resulting in decreased Fe(III) mineral precipitation. At the same time due to decreasing temperature the replenishment with regards to silica slows down and eventually as the temperature gets too cold, amorphous silica starts to precipitate. Meanwhile, the Fe(II) reservoir, which was mostly depleted by the activity of the photoferrotrophs during summer starts to be increased again. In **winter**, due to oversaturation with regards to silica, extensive silica precipitation and formation of Si-rich layers takes place. Silica precipitation stops once the silica concentration drops below the equilibrium value at low temperature. Meanwhile, due to the inactivity of the photoferrotrophs, the Fe(II) reservoir is replenished. In **spring**, due to higher temperature no more silica is being precipitated, allowing both the Fe(II) and silica reservoirs to continue and start to be refilled, respectively. Once the temperature gets high enough the photoferrotrophs become re-activated and they start oxidizing Fe(II). (For interpretation of the references to color in this figure legend, the reader is referred to the web version of this article.)

underlying mechanism(s) and to support our hypothesis that organics formed by microorganisms caused the decreased removal of silica from solution, we performed SEM analysis,  $\zeta$ -potential measurements, and potentiometric titrations of the Fe(III) mineral-cell aggregates.

SEM micrographs showed that *R. iodosum* cells are generally closely associated with the Fe(III) minerals. Natural organic matter (NOM) and EPS are known to have a strong affinity towards Fe(III) (oxyhydr)oxides (Gu et al., 1994; Phoenix et al., 2003; Amstaetter et al., 2012; Shimizu et al., 2013; Hao et al., 2016; Sundman et al., 2017), which suggests that the cells and/or EPS produced by *R. iodosum* (Wu et al., 2014) bind iron as well and might significantly influence the characteristics of the Fe(III) minerals formed and the extent to which Fe(III) minerals and silica are co-precipitated. Indeed,  $\zeta$ -potential measurements showed that the presence of biomass significantly lowered the surface charge of the Fe(III) mineral-cell aggregates ( $-23.5 \pm 1.4$  mV) compared to an abiotic Fe(III) mineral ( $-16.3 \pm 0.7$  mV). This is most likely related to carboxyl/phosphodiester groups as identified by our titration experiments, and previously demonstrated by Martinez et al. (2016), which make the surface of the Fe(III) mineral-cell aggregates more negative. It has been previously shown that NOM or humic substances can lower the  $\zeta$ -potential of e.g. hydrous Al oxides or ferrihydrite significantly, when sorbed to or co-precipitated with such minerals (Pommerenk and Schafran, 2005; Angelico et al., 2014). Furthermore, the sorption of other anions, such as phosphate, was shown to be decreased by up to 40% in NOM-containing systems compared to NOM-free systems (Davis, 1982). Consequently, our experimental results suggest that the reaction of organic matter produced by *R. iodosum*, together with Fe(III) minerals, lowers the surface charge of the Fe(III) mineral-cell aggregates, making them more negatively-charged. Based on these experimental results it would be expected for any anion to be electrostatically repulsed by the negatively charged surface. Yet based on our modelling results >99% of the silica should be present as  $\text{Si}(\text{OH})_4$  which is the predominant species at  $\text{pH} < 9$  (e.g. Sjöberg, 1996; Tan et al., 2013). Nevertheless, despite deprotonation at high pH values, silica still possesses a point of zero charge of 3 due to external silanol groups (Williams and Crerar, 1985). Consequently, dissolved silica should have a residual negative surface charge under our experimental conditions resulting in some electrostatic repulsion between the Fe(III) minerals surface and silica oligo- and polymers which potentially formed. Furthermore, it has been determined that silica dimers ( $\text{H}_5\text{Si}_2\text{O}_7$ ) have a  $\text{pK}_a$  value of  $-5.0$  (Svensson et al., 1986; Felmy et al., 2001), suggesting a significant part of negatively-charged dimers being present in aquatic systems. Another relevant process is the blocking of hydroxyl groups responsible for the formation of Fe-O-Si linkages (Carlson and Schwertmann, 1981; Doelsch et al., 2001) and the sorption of silica to Fe(III) minerals by bidentate, binuclear linkages (Pokrovski et al., 2003; Hiemstra et al., 2007; Swedlund et al., 2010). Irrespective of the exact process, we suggest that co-precipitated organic matter would inhibit the sorption of silica to the Fe(III) mineral-cell aggregates

and, therefore, lead to the separate deposition of Fe- and Si-rich layers in BIFs (Fig. 9).

Although our experimental data suggest that sorption of microbially-derived organic matter to the Fe(III) (oxyhydr)oxide minerals would have reduced, or even prevented, sorption and co-precipitation of silica, some uncertainties remain. Strikingly, the first and second warm periods show a different silica-co-precipitation behavior. During the first warm period between 36% and 47% of the dissolved monomeric silica was co-precipitated or sorbed with the Fe(III) minerals during microbial Fe(II) oxidation, while in the second warm period virtually no silica co-precipitation was observed. Based on results for the initial Fe(II) oxidation of the first warm period, Fe- and silica-precipitation would not be independent and the Fe(III) (oxyhydr)oxides act as a shuttle for silica (Fischer and Knoll, 2009). Unfortunately, due to experimental restrictions, the Fe(II) concentrations used in the present study (several mM) were an order of magnitude higher than estimated for the Archean ocean ( $\sim 0.5$  mM  $\text{Fe}^{2+}$ ; Holland, 1973; Morris, 1993). For comparison, Konhauser et al. (2007) had  $\text{Fe}^{2+}$  concentrations two times lower and the concentrations used by Posth et al. (2008) were approximately 7 times lower than in the present study. In both studies silica was only co-precipitated with the Fe(III) minerals to a minor extent, which suggests that silica-co-precipitation is dependent on the initial Fe:Si ratio.

During the initial Fe(II) oxidation step during the first warm period 3.5 mM  $\text{Fe}^{2+}$  were completely oxidized (until day 13, Fig. 2). Upon addition of new medium on days 13, 21, 29 and 43 (Fig. 2), the amount of  $\text{Fe}^{2+}$  added was only between 2.0 and 2.5 mM. This relatively lower amount of  $\text{Fe}^{2+}$  being completely oxidized resulted in the amount of silica being co-precipitated to decrease from initially approximately 50% (day 0–13, Fig. 2) to below 40% (days 13–17, 21–27, 29–35, 43–48; Fig. 2). Thus, at higher initial  $\text{Fe}^{2+}$  concentrations the organics formed were unable to block all the sorption sites for the silica. Consequently, a comparably low removal of between 40% and 50% monomeric silica from solution could represent a contribution of sorption of microbially-derived biomolecules to the decreased drawdown of silica with biogenic ferrihydrite. Throughout the second warm period (day 133–168, Fig. 2) maximum  $\text{Fe}^{2+}$  concentrations were only at around 0.9 mM (Fig. 2) and, therefore, much lower than during the first warm period (2.0–3.5 mM  $\text{Fe}^{2+}$ , Fig. 2). Importantly, no silica co-precipitation was noted during the second warm period, despite the  $\text{Fe}^{2+}$  being completely oxidized. This further confirms the hypothesis that at higher initial  $\text{Fe}^{2+}$  concentrations, the cell-derived organics are not able to block all sorption sites for silica, resulting in an increased co-precipitation of silica and Fe(III) minerals, whereas at low  $\text{Fe}^{2+}$  concentrations, directly relevant for Archean oceans, all surface sites at the Fe(III) (oxyhydr)oxide particles are covered by organics and minimal silica-removal is observed. Consequently, the initially observed high silica co-precipitation would represent an experimental bias, not representative for the overall mechanism as assumed for the Archean ocean where photoferrotophths would have contributed to BIF deposition.

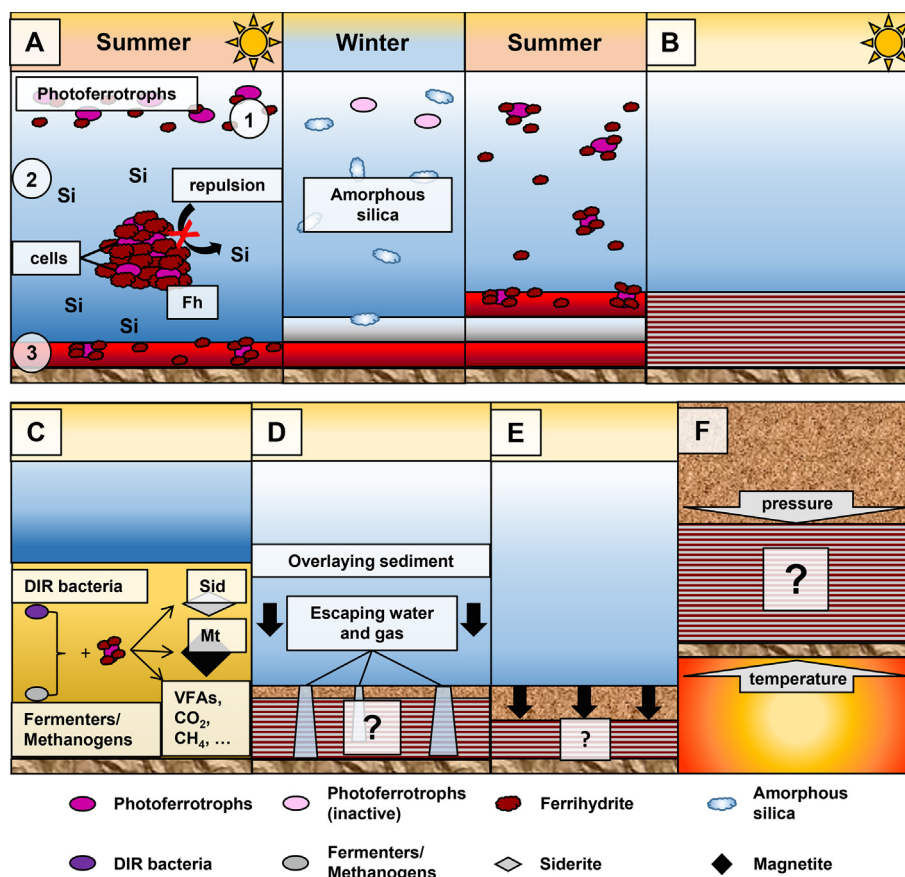


Fig. 9. Overview of diagenetic history of mineral layering in BIFs. (A) Photoferrotrophs are metabolically active during summer and/or warm periods and oxidize  $\text{Fe}^{2+}$  (1). This leads to the formation Fe(III) minerals and the co-precipitation of Fe(III) mineral-cell aggregates, where the co-precipitated/sorbed biomass prevents the silica from being bound to the freshly formed Fe(III) minerals (2). Accumulation of Fe(III) mineral-cell aggregates leads to the formation of Fe-rich layers during warm periods (3). During winter/cold periods the photoferrotrophs become metabolically inactive, leading either to decreased Fe(II) oxidation or completely inhibiting it. Due to the lower solubility at lower temperatures amorphous silica spontaneously precipitates from the water column, thereby forming Si-rich layers. Upon increasing temperature, the photoferrotrophs become active again, leading to renewed Fe(II) oxidation and formation of Fe-rich layers. (B) Over several  $10^5$  to  $10^6$  years of repetitive warm and cold periods or seasons lead to the formation of layered primary BIF sediments. (C) After deposition of Fe(III) mineral-cell aggregates, the co-precipitated biomass is degraded by fermenting bacteria and methanogens, thereby supplying the necessary organic substrates (volatile fatty acids, VFAs) for microbial Fe(III) reduction (DIR), leading to the formation of secondary minerals, such as siderite and magnetite. (D & E) The pressure of overlying sediment layers leads to the compaction and burial of the BIF sediments, probably accompanied by (vertical) escape of pore water and or gases (D), silicification of the silica layers and beginning formation of secondary (Fe) minerals. (F) Upon deep burial, late-stage diagenesis and low-grade metamorphism lead to the formation of secondary Fe minerals, such as siderite, magnetite and hematite. Depending on the previous diagenetic history, the banding should remain stable under these conditions.

Overall, we propose a model where Fe(III) minerals are co-precipitated as aggregates with cells, cell debris, and other organic compounds such as EPS. These organic compounds influence the surface of the aggregates in that they turn them more negative or block surface functional groups of the Fe(III) minerals. This ultimately results in the inhibition of silica sorption leading to a separate deposition of Fe- and Si-rich layers in BIFs (Fig. 9).

#### 4.4. Varve-like deposition of alternating Fe- and Si-rich layers in the Hamersley BIF as a result of temperature cycles

Extended temperature cycling experiments were conducted in order to determine whether the initial model pro-

posed by Posth et al. (2008) could have resulted in the alternating deposition of Fe- and Si-rich layers in BIFs. The experimental setup aimed at simulating the Archean ocean as closely as possible and showed that temperature cycles linking photoferrotrophy during warm periods to abiotic silica precipitation during cold periods results in the development of alternating layers of Fe(III) and silica minerals, similar to those found as microbands in BIFs. However, some of the experimental conditions (determined by constraints due to the chosen experimental setup), namely full light saturation and comparably high  $\text{Fe}^{2+}$  concentrations (low mM range) are potentially at odds with the depositional conditions assumed for the Archean ocean. However, although we conducted our experiments under

full light conditions and specifically envision an ocean devoid of free oxygen, where there would have been no need for photoferrotrophs to move deeper into the water column in order to be able to compete with other Fe(II)-oxidizing mechanisms, it has been suggested that photoferrotrophs could have even been active at lower light intensities at approximately 100 m water depth (Kappler et al., 2005). We, therefore, took a more conservative approach to investigate the minimum requirements under which photoferrotrophs could still deposit BIFs, while still being able to draw important conclusions regarding the potential mechanisms being responsible for the alternating deposition of Fe- and Si-rich layers in BIFs.

In order to quantify whether our proposed model would still be of significance for BIF deposition under the relevant conditions discussed above, we extrapolated our experimental results to the rock record, focusing on the Hamersley Group in Western Australia. The Fe(II) oxidation rates obtained from the first warm periods were determined from Fe(II) concentrations one order of magnitude higher than assumed for the Archean ocean. Therefore, we specifically focused on the Fe(II) oxidation rates determined for the second warm period where the Fe(II) concentrations (~0.8–0.9 mM) were of the same order of magnitude as in the Archean ocean and consequently the data obtained would be more comparable. Furthermore, we adjusted the Fe(II) oxidation rates used to low light intensity values (as outlined below) to showcase that photoferrotrophs might have been active deeper in the water column of the Archean ocean. The key variables for the following calculations are summarized in Table 4.

One requirement for the deposition of Fe-rich layers is the supply of Fe(II) at rates sufficient to sustain ongoing Fe(II) oxidation. Assuming that the Hamersley Basin can be approximated by a simple box we calculated a theoretical layer thickness for a photoferrotrophic community required to oxidize all Fe(II) before it reaches the surface of the ocean based on Kappler et al. (2005). Further assuming the maximum Fe<sup>2+</sup> concentration in the Archean was 0.5 mM (Holland, 1973; Morris, 1993), using an adapted Fe(II) oxidation rate of 0.04 mM d<sup>-1</sup> and the theoretically predicted eddy diffusion coefficient for the modern ocean (as given in Kappler et al., 2005), the photoferrotrophic community would have a uniform thickness of 10.4 m over the whole basin (Table 4). Furthermore, based on the

oxidation rate given and the total volume of water contained in this photoferrotrophic community layer stretched over the entire basin, 5.6 \* 10<sup>10</sup> mol Fe(II) d<sup>-1</sup> would be oxidized by a *R. iodosum* community. Using the Fe<sup>2+</sup> concentration given in Table 4 and the volume of the layer, we calculated the total Fe<sup>2+</sup> initially contained in this layer to be 7 \* 10<sup>11</sup> mol. Therefore, the amount of Fe<sup>2+</sup> oxidized by a *R. iodosum* community would equal 8% of the total Fe<sup>2+</sup> present in the respective layer being oxidized each day. Again assuming that the basin can be approximated by a simple box, applying this 8% to the layer thickness of the photoferrotrophic community (10.4 m) would result in a ca. 0.8 m thick part of this layer (8% of 10.4 m) being depleted in Fe<sup>2+</sup> each day. Assuming homogeneous Fe<sup>2+</sup> distribution, Fe(II) oxidation and upwelling, an upwelling rate of ca. 0.8 m d<sup>-1</sup> would be required to sustain continuous Fe(II) oxidation. This calculated value is within the same order of magnitude as upwelling rates observed in modern upwelling areas (up to 3.0 m d<sup>-1</sup>; Kadko and Johns, 2011; Kadko, 2017), supporting the plausibility of the assumptions made.

Based on this calculation, it seems feasible that photoferrotrophs could have continuously oxidized Fe<sup>2+</sup> in an Archean ocean during warm periods (Fig. 9A.1). Additionally, it needs to be determined whether the amount of Fe<sup>2+</sup> oxidized would have been sufficient to ultimately result in the BIF layer thicknesses observed today. The 5.6 \* 10<sup>10</sup> mol Fe<sup>2+</sup> oxidized by *R. iodosum* each day would correspond to 2.04 \* 10<sup>13</sup> mol Fe<sup>2+</sup> being oxidized each year. Based on a molar mass of 107 g mol<sup>-1</sup> for ferrihydrite (Fe(OH)<sub>3</sub>), this would correspond to 2.18 \* 10<sup>15</sup> g ferrihydrite yr<sup>-1</sup> deposited over the whole Hamersley basin or 2.18 \* 10<sup>4</sup> g ferrihydrite m<sup>-2</sup> yr<sup>-1</sup>. Based on a previously determined density of 2 g cm<sup>-3</sup> (2 \* 10<sup>6</sup> g m<sup>-3</sup>) for Fe(III) mineral-cell aggregates (Posth et al., 2010), this would result in a yearly deposited layer thickness of 0.0109 m yr<sup>-1</sup> or 10.9 mm yr<sup>-1</sup> in the initial sediment (Fig. 9A.3); this is one magnitude higher than calculated by Konhauser et al. (2002) and Kappler et al. (2005) but can be attributed to slightly higher Fe(II) oxidation rates.

After having determined that a photoferrotrophic community would have been able to deposit a sufficiently thick primary Fe(III) mineral layer, it remains to be determined whether the seasonal cooling of the Archean ocean could have resulted in the deposition of silica layers which would

Table 4  
Variables used for verification of the temperature cycling model.

Variable		Reference
Hamersley depositional area	10 <sup>11</sup> m <sup>2</sup>	Konhauser et al. (2002)
Average depth of Hamersley basin	500 m	Trendall (2002)
Depth of seasonal thermocline	100 m	Pinet (2011)
Photoc depth	100 m	Pinet (2011)
Fe <sup>2+</sup> concentration	0.02–0.5 mM	Holland (1973); Morris (1993)
Fe(II) oxidation rate	0.2 mM d <sup>-1</sup>	Experimental data
Fe(II) oxidation rate at 20% efficiency	0.04 mM d <sup>-1</sup>	Adapted from Kappler et al. (2005)
Layer thickness of photoferrotrophic community	10.4 m	Calculated following Kappler et al. (2005)

ultimately be of comparable layer thicknesses as found in BIFs today. However, because the silica concentrations necessary to precipitate amorphous silica, the scale, and the duration of our experiments were so fundamentally different from what is assumed for the Archean ocean, the following paragraphs containing discussion on silica precipitation should be seen as a thought experiment only. Nonetheless, with regards to the maximum amount of silica being precipitated during the cool-down of the ocean the 0.5 mM difference between the silica concentration determined experimentally during the second warm period (ca. 2.1 mM) and the cold period (ca. 1.6 mM), values comparable to known literature values for silica solubility at the respective temperatures (Gunnarsson and Arnórsson, 2000), seem to be a reasonable approach. Based on those and literature values, we expect that little or no further amorphous silica is being precipitated once the lower temperature limit is reached. Since we consider temperature as the major driver for the alternating deposition of Fe- and Si-rich layers, only the depth of the ocean which is affected by temperature changes (thermocline at ca. 100 m in modern oceans; Pinet, 2011) will be taken into account for silica precipitation. From the layer affected by seasonal temperature changes extrapolated over the entire basin ( $10^{11} \text{ m}^2$ ),  $0.5 * 10^{13} \text{ mol amorphous silica yr}^{-1}$  ( $50 \text{ mol amorphous silica m}^{-2}$ ) could be deposited during a respective cold period or winter (Fig. 9A). Using the molar mass of  $60 \text{ g mol}^{-1}$  for  $\text{SiO}_2$  this would result in a yearly precipitation of  $3 * 10^{14} \text{ g amorphous silica}$  ( $3 * 10^3 \text{ g amorphous silica m}^{-2} \text{ yr}^{-1}$ ). Based on the density for amorphous silica of  $2.2 \text{ g cm}^{-3}$  (Renner and Zemek, 1973) and water a weighted average of  $1.24 \text{ g cm}^{-3}$  (assuming 80% water content) was calculated for the initial silica precipitates. Applying this density, a layer thickness of 2.42 mm was calculated.

Over the course of several  $10^5$ – $10^6$  years alternating warm and cold periods could have resulted in the formation of layered primary sediments (Fig. 9B). However, once the initial wet, unconsolidated Fe(III)-rich sedimentary layers were deposited, several post-depositional processes would have changed the layer thickness. On the one hand there were microbial processes. Konhauser et al. (2005) suggested that 70% of the initially precipitated Fe(III) minerals might have been reduced by Fe(II)-reducing bacteria and cycled back into the water column (Fig. 9C). Therefore, the calculated layer thickness for the Fe(III) mineral layers would be reduced from  $10.9 \text{ mm yr}^{-1}$  to  $3.27 \text{ mm yr}^{-1}$ . Furthermore, taking into account that the initially precipitated Fe-rich sediments were compacted by the mass of overlying sediment layers (Fig. 9D and E), the Fe-layer thickness would be further reduced by 75% (Altermann and Nelson, 1998) to  $0.82 \text{ mm yr}^{-1}$ . This value corresponds closely to the mean varve thickness calculated by Trendall and Blockley (1970) of 0.65 mm, and is within one order of magnitude of previous estimates of  $0.033 \text{ mm yr}^{-1}$  compacted BIF sedimentation rate for the Fe-layer (Pickard, 2002).

Similar to the Fe-mineral layers, the silica layers would have been subject to post-depositional processes. Based on our experimental results the silica layers contained more water compared to the Fe(III) mineral layers (Fig. 1). This

is further supported by preliminary experiments where a 2-line ferrihydrite suspension and a monomeric silica solution were added alternately to the marine phototroph medium in experimental tubes and subsequently centrifuged. After centrifugation, the formed amorphous silica layers showed a strong compaction while the formed Fe mineral layers showed only minor compaction (if any at all; data not shown). Consequently, we applied a higher compaction of 95% for the silica layers, as suggested for the compaction of BIFs by Trendall and Blockley (1970). This resulted in the silica layer thickness being reduced from  $2.42 \text{ mm yr}^{-1}$  to  $0.12 \text{ mm yr}^{-1}$ , which is well within the mm to sub-mm range which has been suggested for BIF silica-microbands (Trendall and Blockley, 1970). Additionally, when considering that one Si-rich layer containing up to 50 wt.% of  $\text{SiO}_2$  (Trendall, 2002) was of continuous thickness, stretched laterally over the whole Hamersley area and had an average density of chert ( $2.7 \text{ g cm}^{-3}$ ), it would contain  $1.7 * 10^{13} \text{ g SiO}_2$ . This value is within one order of magnitude of the value calculated based on the temperature-driven decrease of the monomeric silica concentration for a cold period as discussed above, which supports the validity of the assumptions taken for the calculations of the silica layer thicknesses.

In summary, the calculated layer thicknesses for Fe- and Si-rich layers based on the experimental data suggest that biannual temperature changes might have led to the formation of microbands in BIFs (Trendall and Blockley, 1970). Furthermore, we apply the definition of Trendall (2002), where one Fe- and one Si-rich layer together make up one microband and thus represent one year of precipitation, i.e., a chemical varve. Consequently, the layer thickness for both layers would decrease to 0.31 mm and 0.06 mm for the Fe- and Si-rich layers for half a year of deposition, respectively. In combination this would result in  $0.37 \text{ mm}$  compacted yearly sedimentation rate. For  $10^6$  years this would result in a BIF of 370 m vertical extent. Of course, these results only apply when considering that BIFs were deposited continuously without any depositional hiatuses. When assuming varves as mode of deposition for BIFs, the results of our study are within the range of other sedimentation rates found. Trendall and Blockley (1970) estimated the average thickness of one Fe- and silica-layer couplet to be 0.65 mm in the Dales Gorge Member of the Brockman Iron Formation in Western Australia, which would result in a depositional thickness of 650 m after  $10^6$  years. Klein and Beukes (1989) derived a deposition rate of  $570 \text{ m Myr}^{-1}$  for the BIF in the Campbellrand-Kuruman transition zone, Transvaal Supergroup, South Africa, while Morris (1993) estimated the deposition rate of the BIFs of the Hamersley group, Pilbara Craton, Western Australia to have been  $890 \text{ m Myr}^{-1}$ . Other estimates for the same BIF are given by Trendall et al. (2004) with  $180 \text{ m Myr}^{-1}$ . Overall, the values calculated based on our experimental results are well in line with compacted sedimentation rates estimated from the BIF rock record. Accordingly, we suggest that biannual temperature cycles, as originally envisioned by Posth et al. (2008), would have contributed significantly to the deposition of BIFs. Varves would, therefore, have been the most likely mode of deposition for BIFs on the

microband scale, leading to the formation of BIFs as we observe them today.

## 5. CONCLUSIONS

In modern environments, temperature changes play an important role in controlling biologic (microbial) and abiotic processes. Our study suggests that seasonal (or periodical) temperature changes could have played an equally important role in the Archean ocean during the deposition of BIFs. Although temperature changes certainly had a major control over the activity of Fe(II)-oxidizing bacteria (photoferrotrophs), our experimental results provide no conclusive evidence that temperatures as low as 5 °C would have had any direct influence on abiotic silica precipitation. Instead a high degree of silica oversaturation was necessary to form an amorphous silica layer. This is in contrast to some of our experimental results and geochemical modelling which suggest that lower temperatures would have resulted in lower equilibrium concentrations of monomeric silica and ultimately should have resulted in silica precipitation given that a solution is saturated with regards to amorphous silica at 26 °C. Therefore, abiotic silica precipitation is either extremely slow and thus not testable at the experimental (time)scale or for example nucleation points are necessary to initiate silica precipitation.

While the exact mechanism underlying abiotic silica precipitation is currently unknown, we suggest that some coprecipitation of biomass with the Fe(III) minerals occurred and changed the characteristics of the precipitates in a way which prevented sorption of silica to the Fe(III) minerals, thus ultimately causing a separation of Fe- and Si-rich layers in BIFs. To our knowledge this is the first study utilizing marine microbial strains for this kind of BIF deposition simulation experiments and thus confirms that these bacteria could have been active in an anoxic, Fe- and Si-rich Archean ocean. Most importantly, seasonal temperature changes represent a simple unifying mechanism which could have controlled biological and abiotic processes on a basin scale and, therefore, represent a plausible means to explain the large-scale continuity of the banding in BIFs and therefore suggesting the banding in BIFs to be of primary origin.

Although the experimental data suggest that temperature cycles may have contributed significantly to the development of the characteristic lamination in BIFs, it is certain that other processes contributed to the ultimate appearance of Fe- and Si-rich layers in BIFs as we see them today (Fig. 9). For example, not all banding in BIF is on the micron- to millimeter scale, and not all banding is between iron and silica-rich minerals. Moreover, any model on BIF must also take into account the mesobanding and macrobanding which rely on decadal to longer time scales. One important parameter which potentially determined the predominance of either Fe- or Si-rich layers is the supply of Fe<sup>2+</sup> to BIF depositional areas: Higher Fe<sup>2+</sup> fluxes would have resulted in the deposition of dominantly Fe-rich layers and masked silica precipitation, while lower Fe<sup>2+</sup> fluxes would have resulted in a decline or secession

of microbial activity and led to the formation of more and vertically more extensive Si-rich layers. Prolonged warm periods could also have resulted in the predominance and formation of vertically more extensive of Fe-rich layers, while periods of prolonged subaerial volcanism might have favored the formation of vertically more extensive Si-rich layers by suppressing the formation of Fe(III) (oxyhydr)oxides by Fe(II)-metabolizing bacteria. Additionally, a recent study suggested that Milankovitch forcing would have exerted a major control on past climate oscillations on a scale of 0.41 Myr and 1.4 to 1.6 Myr, thereby influencing the composition of BIFs on a large scale (Lantink et al., 2019).

It is also unclear to which extent post-depositional processes altered the initial BIF sediment. Konhauser et al. (2005) suggested that up to 70% of the initial Fe(III) mineral precipitates could have been reduced by microbial activity and cycled back into the water column. This could potentially also have led to a release of silica from the aggregates which could then have been recycled back into the water column. If dissolution took place within the sediment itself, silica could have become concentrated in the pore space, thereby enhancing silicification and consequently either (1) disrupting any clear layering or (2) stabilizing the layering during further diagenesis and metamorphism. Abiogenic diagenetic processes would also have influenced the primary layering. It seems conceivable based on the differences in density between the primary Fe(III) minerals and amorphous silica that the much denser Fe(III) minerals should displace and potentially disrupt any amorphous silica layer. Additionally, it would be expected that the pressure of the overlaying sediment column would lead to the compaction and vertical escape of water and dissolved silica (Fig. 9D and E). In either case it would be required that the silica layers silicify and solidify early during the diagenesis as proposed by Ewers and Morris (1981) in order to remain stable and consistent during the diagenetic history. Last but not least, it is unclear how deep burial and low-grade metamorphism would have influenced the stability of the laminated primary sediment and how the primary layering would have been preserved under such conditions.

## ACKNOWLEDGMENTS

The authors would like to thank Dr. H. Schulz for advice and support with SEM analysis and providing information on seasonal and glacial/inter-glacial temperature changes in modern oceans. Dr. J.M. Byrne is thanked for help with preparation of SEM samples and analysis and interpretation of Moessbauer spectra. M. Maisch is acknowledged for help with analysis of Moessbauer spectra and conducting  $\mu$ XRD analysis. Dr. A. Mloszewska, Dr. W. Wu, Dr. S. Lalonde, Dr. L. Robbins and T. Warchola are further acknowledged for fruitful discussions and advice on the experimental design. This study was supported by grants from the German Research Foundation (DFG) to AK and a Natural Sciences and Engineering Research Council (NSERC) grant to KOK.

## DECLARATION OF INTEREST

None.

## APPENDIX A. SUPPLEMENTARY MATERIAL

Supplementary data to this article can be found online at <https://doi.org/10.1016/j.gca.2019.08.031>.

## REFERENCES

- Alibert C. (2016) Rare earth elements in Hamersley BIF minerals. *Geochim. Cosmochim. Acta* **184**, 311–328.
- Altermann W. and Nelson D. R. (1998) Sedimentation rates, basin analysis and regional correlations of three Neoproterozoic and Palaeoproterozoic sub-basins of the Kaapvaal craton as inferred from precise U-Pb zircon ages from volcanoclastic sediments. *Sediment. Geol.* **120**, 225–256.
- Amstaetter K., Borch T. and Kappler A. (2012) Influence of humic acid imposed changes of ferrihydrite aggregation on microbial Fe (III) reduction. *Geochim. Cosmochim. Acta* **85**, 326–341.
- Angelico R., Ceglie A., He J.-Z., Liu Y.-R., Palumbo G. and Colombo C. (2014) Particle size, charge and colloidal stability of humic acids coprecipitated with ferrihydrite. *Chemosphere* **99**, 239–247.
- Bau M. and Alexander B. W. (2009) Distribution of high field strength elements (Y, Zr, REE, Hf, Ta, Th, U) in adjacent magnetite and chert bands and in reference standards FeR-3 and FeR-4 from the Temagami iron-formation, Canada, and the redox level of the Neoproterozoic ocean. *Precambrian Res.* **174**, 337–346.
- Bekker A., Slack J. F., Planavsky N., Krapež B., Hofmann A., Konhauser K. O. and Rouxel O. J. (2010) Iron formation: the sedimentary product of a complex interplay among mantle, tectonic, oceanic, and biospheric processes. *Econ. Geol.* **105**, 467–508.
- Bekker A., Planavsky N., Rasmussen B., Krapež B., Hofmann A., Slack J., Rouxel O. and Konhauser K. O. (2014) Iron formations: Their origins and implications for ancient seawater chemistry. *Treatise Geochem.* **9**.
- Beukes N. J. (1973) Precambrian iron-formations of southern Africa. *Econ. Geol.* **68**, 960–1004.
- Beukes N. J. (1984) Sedimentology of the Kuruman and griquatown iron-formations, Transvaal supergroup, Griqualand West, South Africa. *Precambrian Res.* **24**, 47–84.
- Bird L. J., Coleman M. L. and Newman D. K. (2013) Iron and copper act synergistically to delay anaerobic growth of bacteria. *Appl. Environ. Microbiol.* **79**, 3619–3627.
- Carlson L. and Schwertmann U. (1981) Natural ferrihydrites in surface deposits from Finland and their association with silica. *Geochim. Cosmochim. Acta* **45**, 421,427–425,429.
- Chan C. S., Emerson D. and Luther, III, G. W. (2016) The role of microaerophilic Fe-oxidizing micro-organisms in producing banded iron formations. *Geobiology* **14**, 509–528.
- Cloud P. E. (1965) Significance of the Gunflint (Precambrian) microflora photosynthetic oxygen may have had important local effects before becoming a major atmospheric gas. *Science* **148**, 27–35.
- Cloud P. E. (1973) Paleocological significance of the banded iron-formation. *Econ. Geol.* **68**, 1135–1143.
- Cornell R. M., Giovanoli R. and Schindler P. W. (1987) Effect of silicate species on the transformation of ferrihydrite into goethite and hematite in alkaline media. *Clays Clay Miner.* **35**, 21–28.
- Cox J. S., Smith D. S., Warren L. A. and Ferris F. G. (1999) Characterizing heterogeneous bacterial surface functional groups using discrete affinity spectra for proton binding. *Environ. Sci. Technol.* **33**, 4514–4521.
- Craddock P. R. and Dauphas N. (2011) Iron and carbon isotope evidence for microbial iron respiration throughout the Archean. *Earth. Planet. Sci. Lett.* **303**, 121–132.
- Crowe S. A., Jones C., Katsev S., Magen C., O'Neill A. H., Sturm A., Canfield D. E., Haffner G. D., Mucci A. and Sundby B. (2008) Photoferrotrophs thrive in an Archean Ocean analogue. *Proc. Natl. Acad. Sci.* **105**, 15938–15943.
- Czaja A. D., Johnson C. M., Beard B. L., Roden E. E., Li W. and Moorbath S. (2013) Biological Fe oxidation controlled deposition of banded iron formation in the ca. 3770Ma Isua Supracrustal Belt (West Greenland). *Earth. Planet. Sci. Lett.* **363**, 192–203.
- Davis J. A. (1982) Adsorption of natural dissolved organic matter at the oxide/water interface. *Geochim. Cosmochim. Acta* **46**, 2381–2393.
- Dimroth E. and Chauvel J. J. (1973) Petrography of the Sokoman iron formation in part of the central Labrador trough, Quebec, Canada. *Geol. Soc. Am. Bull.* **84**, 111–134.
- Doelsch E., Stone W. E., Petit S., Masion A., Rose J., Bottero J.-Y. and Nahon D. (2001) Speciation and crystal chemistry of Fe (III) chloride hydrolyzed in the presence of SiO<sub>4</sub> ligands. 2. Characterization of Si-Fe aggregates by FTIR and <sup>29</sup>Si solid-state NMR. *Langmuir* **17**, 1399–1405.
- Eggseder M., Cruden A. R., Tomkins A. G., Wilson S. A. and Langendam A. D. (2018) Colloidal origin of microbands in banded iron formations. *Geochem. Perspect. Lett.* **6**, 43–49.
- Ehrenreich A. and Widdel F. (1994) Anaerobic oxidation of ferrous iron by purple bacteria, a new type of phototrophic metabolism. *Appl. Environ. Microbiol.* **60**, 4517–4526.
- Eickhoff M., Obst M., Schröder C., Hitchcock A. P., Tyliczszak T., Martinez R. E., Robbins L. J., Konhauser K. O. and Kappler A. (2014) Nickel partitioning in biogenic and abiogenic ferrihydrite: the influence of silica and implications for ancient environments. *Geochim. Cosmochim. Acta* **140**, 65–79.
- Emery W. J., Talley L. D. and Pickard G. L. (2006) *Descriptive physical oceanography*. Elsevier, Amsterdam.
- Ewers W. E. and Morris R. C. (1981) Studies of the Dales Gorge member of the Brockman iron formation, Western Australia. *Econ. Geol.* **76**, 1929–1953.
- Felny A. R., Cho H., Rustard J. R. and Mason M. J. (2001) An aqueous thermodynamic model for polymerized silica species to high ionic strength. *J. Solution Chem.* **30**, 509–525.
- Fischer W. W. and Knoll A. H. (2009) An iron shuttle for deepwater silica in Late Archean and early Paleoproterozoic iron formation. *Geol. Soc. Am. Bull.* **121**, 222–235.
- Frei R. and Polat A. (2007) Source heterogeneity for the major components of ~3.7 Ga Banded Iron Formations (Isua Greenstone Belt, Western Greenland): tracing the nature of interacting water masses in BIF formation. *Earth. Planet. Sci. Lett.* **253**, 266–281.
- Galili N., Shemesh A., Yam R., Brailovsky I., Sela-Adler M., Schuster E. M., Collom C., Bekker A., Planavsky N., Macdonald F. A., Pr at A., Rudmin M., Trela W., Stuesson U., Heikoop J. M., Aurell M., Ramajo J. and Halevy I. (2019) The geologic history of seawater oxygen isotopes from marine iron oxides. *Science* **365**, 469–473.
- Gauger T., Konhauser K. O. and Kappler A. (2015) Protection of phototrophic iron (II)-oxidizing bacteria from UV irradiation by biogenic iron (III) minerals: implications for early Archean banded iron formation. *Geology* **43**, 1067–1070.
- Gauger T., Byrne J. M., Konhauser K. O., Obst M., Crowe S. and Kappler A. (2016) Influence of organics and silica on Fe (II)

- oxidation rates and cell–mineral aggregate formation by the green-sulfur Fe (II)-oxidizing bacterium *Chlorobium ferrooxidans* KoFox—Implications for Fe (II) oxidation in ancient oceans. *Earth. Planet. Sci. Lett.* **443**, 81–89.
- Gu B., Schmitt J., Chen Z., Liang L. and McCarthy J. F. (1994) Adsorption and desorption of natural organic matter on iron oxide: mechanisms and models. *Environ. Sci. Technol.* **28**, 38–46.
- Gunnarsson I. and Arnórsson S. (2000) Amorphous silica solubility and the thermodynamic properties of  $H_4SiO_4$  in the range of 0 to 350 C at Psat. *Geochim. Cosmochim. Acta* **64**, 2295–2307.
- Halama M., Swanner E. D., Konhauser K. O. and Kappler A. (2016) Evaluation of siderite and magnetite formation in BIFs by pressure–temperature experiments of Fe(III) minerals and microbial biomass. *Earth. Planet. Sci. Lett.* **450**, 243–253.
- Halevy I. and Bachan A. (2017) The geologic history of seawater pH. *Science* **355**, 1069–1071.
- Hamade T., Konhauser K. O., Raiswell R., Goldsmith S. and Morris R. C. (2003) Using Ge/Si ratios to decouple iron and silica fluxes in Precambrian banded iron formations. *Geology* **31**, 35–38.
- Hao L., Guo Y., Byrne J. M., Zeitvogel F., Schmid G., Ingino P., Li J., Neu T. R., Swanner E. D. and Kappler A. (2016) Binding of heavy metal ions in aggregates of microbial cells, EPS and biogenic iron minerals measured in-situ using metal-and glycoconjugates-specific fluorophores. *Geochim. Cosmochim. Acta* **180**, 66–96.
- Hartman H. (1984) *The evolution of photosynthesis and microbial mats: A speculation on the banded iron formations*. MBL LECT, BIOL.
- Hashizume K., Pinti D. L., Orberger B., Cloquet C., Jayananda M. and Soyama H. (2016) A biological switch at the ocean surface as a cause of laminations in a Precambrian iron formation. *Earth. Planet. Sci. Lett.* **446**, 27–36.
- Herbelin A.L. and Westall J.C. FITEQL 4.0: A computer program for determination of chemical equilibrium constants from experimental data, 1999.
- Hegler F., Posth N. R., Jiang J. and Kappler A. (2008) Physiology of phototrophic iron (II)-oxidizing bacteria: implications for modern and ancient environments. *FEMS Microbiol. Ecol.* **66**, 250–260.
- Heimann A., Johnson C. M., Beard B. L., Valley J. W., Roden E. E., Spicuzza M. J. and Beukes N. J. (2010) Fe, C, and O isotope compositions of banded iron formation carbonates demonstrate a major role for dissimilatory iron reduction in ~2.5 Ga marine environments. *Earth. Planet. Sci. Lett.* **294**, 8–18.
- Hiemstra T., Barnett M. O. and van Riemsdijk W. H. (2007) Interaction of silicic acid with goethite. *J. Colloid Interface Sci.* **310**, 8–17.
- Hohmann C., Winkler E., Morin G. and Kappler A. (2009) Anaerobic Fe(II)-oxidizing bacteria show As resistance and immobilize As during Fe (III) mineral precipitation. *Environ. Sci. Technol.* **44**, 94–101.
- Holland H. D. (1973) The oceans; a possible source of iron in iron-formations. *Econ. Geol.* **68**, 1169–1172.
- Holm N. G. (1987) Biogenic influences on the geochemistry of certain ferruginous sediments of hydrothermal origin. *Chem. Geol.* **63**, 45–57.
- Iler R. K. (1979) *The chemistry of silica: solubility, polymerization, colloid and surface properties, and biochemistry*. Wiley.
- Isley A. E. (1995) Hydrothermal plumes and the delivery of iron to banded iron formation. *J. Geol.*, 169–185.
- Isley A. E. and Abbott D. H. (1999) Plume-related mafic volcanism and the deposition of banded iron formation. *J. Geophys. Res. : Solid Earth* **1978–2012**(104), 15461–15477.
- Johnson J. E., Muhling J. R., Cosmidis J., Rasmussen B. and Templeton A. S. (2018) Low-Fe(III) greenalite was a primary mineral from neoproterozoic oceans. *Geophys. Res. Lett.* **45**, 3182–3192.
- Jones A. M., Collins R. N., Rose J. and Waite T. D. (2009) The effect of silica and natural organic matter on the Fe (II)-catalysed transformation and reactivity of Fe (III) minerals. *Geochim. Cosmochim. Acta* **73**, 4409–4422.
- Jones C., Nomosatryo S., Crowe S. A., Bjerrum C. J. and Canfield D. E. (2015) Iron oxides, divalent cations, silica, and the early earth phosphorus crisis. *Geology* **43**, 135–138.
- Kadko D. (2017) Upwelling and primary production during the US GEOTRACES East Pacific Zonal Transect. *Glob. Biogeochem. Cycles* **31**, 218–232.
- Kadko D. and Johns W. (2011) Inferring upwelling rates in the equatorial Atlantic using  $^7\text{Be}$  measurements in the upper ocean. *Deep Sea Res. Part I: Oceanogr. Res. Pap.* **58**, 647–657.
- Kappler A. and Newman D. K. (2004) Formation of Fe (III)-minerals by Fe (II)-oxidizing photoautotrophic bacteria. *Geochim. Cosmochim. Acta* **68**, 1217–1226.
- Kappler A., Pasquero C., Konhauser K. O. and Newman D. K. (2005) Deposition of banded iron formations by anoxygenic phototrophic Fe (II)-oxidizing bacteria. *Geology* **33**, 865–868.
- Kasting J. F., Howard M. T., Wallmann K., Veizer J., Shields G. and Jaffrés J. (2006) Paleoclimates, ocean depth, and the oxygen isotopic composition of seawater. *Earth. Planet. Sci. Lett.* **252**, 82–93.
- Klein C. (2005) Some Precambrian banded iron-formations (BIFs) from around the world: Their age, geologic setting, mineralogy, metamorphism, geochemistry, and origins. *Am. Mineral.* **90**, 1473–1499.
- Klein C. and Beukes N. J. (1989) Geochemistry and sedimentology of a facies transition from limestone to iron-formation deposition in the early Proterozoic Transvaal Supergroup, South Africa. *Econ. Geol.* **84**, 1733–1774.
- Klein C. and Beukes N. J. (1992) Time distribution, stratigraphy, and sedimentologic setting, and geochemistry of Precambrian iron-formations. In *The Proterozoic Biosphere: A Multidisciplinary Study* (eds. J. W. Schopf and C. Klein). Cambridge Univ. Press, New York, pp. 139–146.
- Koeksoy E., Halama M., Konhauser K. O. and Kappler A. (2015) Using modern ferruginous habitats to interpret Precambrian banded iron formation deposition. *Int. J. Astrobiol.*, 1–13.
- Koeksoy E., Sundman A., Byrne J. M., Lohmayer R., Planer-Friedrich B., Halevy I., Konhauser K. O. and Kappler A. (2019) Formation of green rust and elemental sulfur in an analogue for oxygenated ferro-euxinic transition zones of Precambrian oceans. *Geology* **47**, 211–214.
- Konhauser K. O., Hamade T., Raiswell R., Morris R. C., Ferris F. G., Southam G. and Canfield D. E. (2002) Could bacteria have formed the Precambrian banded iron formations?. *Geology* **30**, 1079–1082.
- Konhauser K. O., Newman D. K. and Kappler A. (2005) The potential significance of microbial Fe (III) reduction during deposition of Precambrian banded iron formations. *Geobiology* **3**, 167–177.
- Konhauser K. O., Amskold L., Lalonde S. V., Posth N. R., Kappler A. and Anbar A. (2007) Decoupling photochemical Fe (II) oxidation from shallow-water BIF deposition. *Earth. Planet. Sci. Lett.* **258**, 87–100.
- Konhauser K. O., Planavsky N. J., Hardisty D. S., Robbins L. J., Warchola T. J., Haugaard R., Lalonde S. V., Partin C. A., Onk P. B. H., Tsikos H., Lyons T. W., Bekker A. and Johnson C. M. (2017a) Iron formations: A global record of Neoproterozoic to Palaeoproterozoic environmental history. *Earth-Sci. Rev.* **172**, 140–177.

- Konhauser K. O., Robbins L. J., Alessi D. S., Flynn S. L., Gingras M. K., Martinez R. E., Kappler A., Swanner E. D., Li Y.-L. and Crowe S. A. (2017b) Phytoplankton contributions to the trace-element composition of Precambrian banded iron formations. *Geol. Soc. Am. Bull.* **130**, 941–951.
- Krapež B., Barley M. E. and Pickard A. L. (2003) Hydrothermal and resedimented origins of the precursor sediments to banded iron formation: sedimentological evidence from the Early Palaeoproterozoic Brockman Supersequence of Western Australia. *Sedimentology* **50**, 979–1011.
- Krauskopf K. B. (1956) Dissolution and precipitation of silica at low temperatures. *Geochim. Cosmochim. Acta* **10**, 1–26.
- Krissansen-Totton J., Arney G. N. and Catling D. C. (2018) Constraining the climate and ocean pH of the early Earth with a geological carbon cycle model. *Proc. Natl. Acad. Sci.* **115**, 4105–4110.
- Lantink M. L., Davies J. H., Mason P. R., Schaltegger U. and Hilgen F. J. (2019) Climate control on banded iron formations linked to orbital eccentricity. *Nat. Geosci.* **12**, 369–374.
- Larese-Casanova P., Haderlein S. B. and Kappler A. (2010) Biomineralization of lepidocrocite and goethite by nitrate-reducing Fe (II)-oxidizing bacteria: effect of pH, bicarbonate, phosphate, and humic acids. *Geochim. Cosmochim. Acta* **74**, 3721–3734.
- Laufer K., Niemeyer A., Nikeleit V., Halama M., Byrne J. M. and Kappler A. (2017) Physiological characterization of a halotolerant anoxygenic phototrophic Fe(II)-oxidizing green-sulfur bacterium isolated from a marine sediment. *FEMS Microbiol. Ecol.* **93**, fix054.
- Li Y.-L. (2014) Micro- and nanobands in late Archean and Palaeoproterozoic banded-iron formations as possible mineral records of annual and diurnal depositions. *Earth. Planet. Sci. Lett.* **391**, 160–170.
- Li Y.-L., Konhauser K. O., Cole D. R. and Phelps T. J. (2011) Mineral ecophysiological data provide growing evidence for microbial activity in banded-iron formations. *Geology* **39**, 707–710.
- Li Y.-L., Konhauser K. O., Kappler A. and Hao X.-L. (2013) Experimental low-grade alteration of biogenic magnetite indicates microbial involvement in generation of banded iron formations. *Earth. Planet. Sci. Lett.* **361**, 229–237.
- Li Y.-L., Konhauser K. O. and Zhai M. (2017) The formation of magnetite in the early Archean oceans. *Earth. Planet. Sci. Lett.* **466**, 103–114.
- Liu Y., Alessi D., Owttrim G., Petrash D., Mloszewska A., Lalonde S., Martinez R., Zhou Q. and Konhauser K. (2015) Cell surface reactivity of *Synechococcus* sp. PCC 7002: implications for metal sorption from seawater. *Geochim. Cosmochim. Acta* **169**, 30–44.
- Maliva R. G., Knoll A. H. and Simonson B. M. (2005) Secular change in the Precambrian silica cycle: insights from chert petrology. *Geol. Soc. Am. Bull.* **117**, 835–845.
- MARGO Project Members (2009) Constraints on the magnitude and patterns of ocean cooling at the Last Glacial Maximum. *Nature Geoscience* **2**, 127–132.
- Martinez R. E., Smith D. S., Kulczycki E. and Ferris F. G. (2002) Determination of intrinsic bacterial surface acidity constants using a Donnan shell model and a continuous pKa distribution method. *J. Colloid Interface Sci.* **253**, 130–139.
- Martinez R. E., Konhauser K. O., Paunova N., Wu W., Alessi D. S. and Kappler A. (2016) Surface reactivity of the anaerobic phototrophic Fe (II)-oxidizing bacterium *Rhodovulum iodolum*: Implications for trace metal budgets in ancient oceans and banded iron formations. *Chem. Geol.* **442**, 113–120.
- Mloszewska A. M., Pecoits E., Cates N. L., Mojzsis S. J., O’Neil J., Robbins L. J. and Konhauser K. O. (2012) The composition of Earth’s oldest iron formations: the Nuvvuagittuq Supracrustal Belt (Québec, Canada). *Earth. Planet. Sci. Lett.* **317**, 331–342.
- Morris R. C. (1993) Genetic modelling for banded iron-formation of the Hamersley Group, Pilbara Craton Western Australia. *Precambrian Res.* **60**, 243–286.
- Morris R. C. and Horwitz R. C. (1983) The origin of the iron-formation-rich Hamersley Group of Western Australia — deposition on a platform. *Precambrian Res.* **21**, 273–297.
- Nealson K. H. and Myers C. R. (1990) Iron reduction by bacteria: a potential role in the genesis of banded iron formations. *Am. J. Sci.* **290**, 35–45.
- Percak-Dennett E. M., Beard B. L., Xu H., Konishi H., Johnson C. M. and Roden E. E. (2011) Iron isotope fractionation during microbial dissimilatory iron oxide reduction in simulated Archean seawater. *Geobiology* **9**, 205–220.
- Pflaumann U., Sarnthein M., Chapman M., d’Abreu L., Funnell B., Huels M., Kiefer T., Maslin M., Schulz H., Swallow J., van Kreveld S., Vautravers M., Vogelsang E. and Weinel M. (2003) Glacial North Atlantic: sea-surface conditions reconstructed by GLAMAP 2000. *Paleoceanography* **18**.
- Phoenix V. R., Konhauser K. O. and Ferris F. G. (2003) Experimental study of iron and silica immobilization by bacteria in mixed Fe-Si systems: Implications for microbial silicification in hot-springs. *Can. J. Earth Sci.* **40**, 1669–1678.
- Pickard A. L. (2002) SHRIMP U-Pb zircon ages of tuffaceous mudrocks in the Brockman Iron Formation of the Hamersley Range, Western Australia\*. *Aust. J. Earth Sci.* **49**, 491–507.
- Pickard A. L., Barley M. E. and Krapež B. (2004) Deep-marine depositional setting of banded iron formation: sedimentological evidence from interbedded clastic sedimentary rocks in the early Palaeoproterozoic Dales Gorge Member of Western Australia. *Sediment. Geol.* **170**, 37–62.
- Pickard G. L. and Emery W. J. (1982) *Descriptive Physical Oceanography: An Introduction*, 4th enlarged ed. Pergamon Press.
- Pinet P. R. (2011) *Invitation to oceanography*. Jones & Bartlett Publishers.
- Pokrovski G. S., Schott J., Farges F. and Hazemann J. L. (2003) Iron(III)-silica interactions in aqueous solution: Insights from X-ray absorption fine structure spectroscopy. *Geochim. Cosmochim. Acta.* **67**, 3559–3573.
- Pommerenk P. and Schafran G. C. (2005) Adsorption of inorganic and organic ligands onto hydrous aluminum oxide: evaluation of surface charge and the impacts on particle and NOM removal during water treatment. *Environ. Sci. Technol.* **39**, 6429–6434.
- Posth N. R., Hegler F., Konhauser K. O. and Kappler A. (2008) Alternating Si and Fe deposition caused by temperature fluctuations in Precambrian oceans. *Nat. Geosci.* **1**, 703–708.
- Posth N. R., Huelin S., Konhauser K. O. and Kappler A. (2010) Size, density and composition of cell–mineral aggregates formed during anoxygenic phototrophic Fe (II) oxidation: Impact on modern and ancient environments. *Geochim. Cosmochim. Acta* **74**, 3476–3493.
- Posth N. R., Konhauser K. O. and Kappler A. (2013) Microbiological processes in banded iron formation deposition. *Sedimentology* **60**, 1733–1754.
- Posth N. R., Canfield D. E. and Kappler A. (2014) Biogenic Fe (III) minerals: from formation to diagenesis and preservation in the rock record. *Earth-Sci. Rev.* **135**, 103–121.
- Poulton S. W. and Canfield D. E. (2011) Ferruginous conditions: a dominant feature of the ocean through Earth’s history. *Elements* **7**, 107–112.
- Rancourt D. G. and Ping J. Y. (1991) Voigt-based methods for arbitrary-shape static hyperfine parameter distributions in Mössbauer spectroscopy. *Nucl. Instrum. Meth. B* **58**, 85–97.

- Rasmussen B., Meier D. B., Krapež B. and Muhling J. R. (2013) Iron silicate microgranules as precursor sediments to 2.5-billion-year-old banded iron formations. *Geology* **41**, 435–438.
- Rasmussen B., Krapež B., Muhling J. R. and Suvorova A. (2015) Precipitation of iron silicate nanoparticles in early Precambrian oceans marks Earth's first iron age. *Geology* **43**, 303–306.
- Rasmussen B., Muhling J. R., Suvorova A. and Krapež B. (2017) Greenalite precipitation linked to the deposition of banded iron formations downslope from a late Archean carbonate platform. *Precambrian Res.* **290**, 49–62.
- Renner O. and Zemek J. (1973) Density of amorphous silicon films. *Czechoslovak J. Phys.* **23**, 1273–1276.
- Robbins L. J., Funk S. P., Flynn S. L., Warchola T. J., Li Z., Lalonde S. V., Rostrom B. J., Smith A. J. B., Beukes N. J., de Kock M. O., Heaman L. M., Alessi D. S. and Konhauser K. O. (2019) Hydrogeological constraints on the formation of Palaeoproterozoic banded iron formations. *Nat. Geosci.* **12**, 558–563.
- Schaedler S., Burkhardt C., Hegler F., Straub K. L., Miot J., Benzerara K. and Kappler A. (2009) Formation of cell-iron-mineral aggregates by phototrophic and nitrate-reducing anaerobic Fe (II)-oxidizing bacteria. *Geomicrobiol. J.* **26**, 93–103.
- Schwertmann U. and Cornell R. M. (2008) *Iron oxides in the laboratory*. John Wiley & Sons.
- Shimizu M., Zhou J., Schröder C., Obst M., Kappler A. and Borch T. (2013) Dissimilatory reduction and transformation of ferrihydrite-humic acid coprecipitates. *Environ. Sci. Technol.* **47**, 13375–13384.
- Sjöberg S. (1996) Silica in aqueous environments. *J. Non Cryst. Solids* **196**, 51–57.
- Smith A. J. B., Beukes N. J. and Gutzmer J. (2013) The composition and depositional environments of Mesoarchean iron formations of the West Rand Group of the Witwatersrand Supergroup, South Africa. *Econ. Geol.* **108**, 111–134.
- Sokolov I., Smith D. S., Henderson G. S., Gorby Y. A. and Ferris F. G. (2001) Cell surface electrochemical heterogeneity of the Fe (III)-reducing bacteria *Shewanella putrefaciens*. *Environ. Sci. Technol.* **35**, 341–347.
- Steinboefel G., von Blanckenburg F., Horn I., Konhauser K. O., Beukes N. J. and Gutzmer J. (2010) Deciphering formation processes of banded iron formations from the Transvaal and the Hamersley successions by combined Si and Fe isotope analysis using UV femtosecond laser ablation. *Geochim. Cosmochim. Acta* **74**, 2677–2696.
- Stookey L. L. (1970) Ferrozine—a new spectrophotometric reagent for iron. *Anal. Chem.* **42**, 779–781.
- Straub K. L., Rainey F. A. and Widdel F. (1999) *Rhodovulum iodolum* sp. nov. and *Rhodovulum robiginosum* sp. nov., two new marine phototrophic ferrous-iron-oxidizing purple bacteria. *Int. J. Syst. Bacteriol.* **49**, 729–735.
- Strickland J. D. H. and Parsons T. R. (1972) *A practical handbook of seawater analysis*. Fisheries Research Board of Canada, 167, Ottawa.
- Sun S., Konhauser K. O., Kappler A. and Li Y.-L. (2015) Primary hematite in Neoproterozoic to Paleoproterozoic oceans. *Geol. Soc. Am. Bull.* **127**, 850–861.
- Sundman A., Byrne J. M., Bauer I., Menguy N. and Kappler A. (2017) Interactions between magnetite and humic substances: redox reactions and dissolution processes. *Geochem. Trans.* **18**, 6.
- Svensson I. L., Sjöberg S. and Öhman L.-O. (1986) Polysilicate equilibria in concentrated sodium silicate solutions. *J. Chem. Society Faraday Trans. 1*(82), 3635–3646.
- Swanner E. D., Mloszewska A. M., Cirpka O. A., Schoenberg R., Konhauser K. O. and Kappler A. (2015a) Modulation of oxygen production in Archean oceans by episodes of Fe (II) toxicity. *Nat. Geosci.* **8**, 126–130.
- Swanner E. D., Wu W., Schoenberg R., Byrne J., Michel F. M., Pan Y. and Kappler A. (2015b) Fractionation of Fe isotopes during Fe (II) oxidation by a marine photoferrotoph is controlled by the formation of organic Fe-complexes and colloidal Fe fractions. *Geochim. Cosmochim. Acta* **165**, 44–61.
- Swedlund P. J., Miskelly G. M. and McQuillan A. J. (2010) Silicic Acid Adsorption and Oligomerization at the Ferrihydrite-Water Interface: interpretation of ATR-IR Spectra Based on a Model Surface Structure. *Langmuir* **26**, 3394–3401.
- Tan H., Skinner W. and Addai-Mensah J. (2013) PH-mediated interfacial chemistry and particle interactions in aqueous chlorite dispersions. *Chem. Eng. Res. Des.* **91**, 448–456.
- ThomasArrigo L. K., Mikutta C., Byrne J. M., Kappler A. and Kretzschmar R. (2017) Iron (II)-catalyzed iron atom exchange and mineralogical changes in iron-rich organic freshwater flocs: an iron isotope tracer study. *Environ. Sci. Technol.* **51**, 6897–6907.
- ThomasArrigo L. K., Byrne J. M., Kappler A. and Kretzschmar R. (2018) Impact of organic matter on iron (II)-catalyzed mineral transformations in ferrihydrite-organic matter coprecipitates. *Environ. Sci. Technol.* **52**, 12316–12326.
- Toner B. M., Berquó T. S., Michel F. M., Sorensen J. V., Templeton A. S. and Edwards K. J. (2012) Mineralogy of iron microbial mats from Loihi Seamount. *Front Microbiol* **3**, 118.
- Tosca N. J., Guggenheim S. and Pufahl P. K. (2016) An authigenic origin for Precambrian greenalite: Implications for iron formation and the chemistry of ancient seawater. *Geol. Soc. Am. Bull.* **128**, 511–530.
- Trendall A. F. (2002) The significance of iron-formation in the Precambrian stratigraphic record. *Precambrian Sediment. Environ. Modern Approach Depositional Syst. Spec. Publ. Internat. Assoc. Sedimentol.* **33**, 33–66.
- Trendall A. F. and Blockley J. B. (1970) The iron formations of the Hamersley Group, Western Australia, with special reference to the associated crocidolite. *Western Austr. Surv. Bull.* **119**, 353.
- Trendall A. F., Compston W., Nelson D. R., De Laeter J. R. and Bennett V. C. (2004) SHRIMP zircon ages constraining the depositional chronology of the Hamersley Group, Western Australia\*. *Aust. J. Earth Sci.* **51**, 621–644.
- Viehmann S., Hoffmann J. E., Münker C. and Bau M. (2014) Decoupled Hf-Nd isotopes in Neoproterozoic seawater reveal weathering of emerged continents. *Geology* **42**, 115–118.
- Walker J. C. (1984) Suboxic diagenesis in banded iron formations. *Nature* **309**, 340–342.
- Walter X. A., Picazo A., Miracle M. R., Vicente E., Camacho A., Aragno M. and Zopf J. (2014) Phototrophic Fe (II)-oxidation in the chemocline of a ferruginous meromictic lake. *Front. Microbiol.* **5**, 713.
- Widdel F., Schnell S., Heising S., Ehrenreich A., Assmus B. and Schink B. (1993) Ferrous iron oxidation by anoxygenic phototrophic bacteria. *Nature* **362**, 834–836.
- Williams L. A. and Crerar D. A. (1985) Silica diagenesis; II, general mechanisms. *J. Sediment. Res.* **55**, 312–321.
- Williams L. A., Parks G. A. and Crerar D. A. (1985) Silica diagenesis; I, solubility controls. *J. Sediment. Res.* **55**, 301–311.
- Wu W., Swanner E. D., Hao L., Zeitvogel F., Obst M., Pan Y. and Kappler A. (2014) Characterization of the physiology and cell-mineral interactions of the marine anoxygenic phototrophic Fe (II) oxidizer *Rhodovulum iodolum*—implications for Precambrian Fe (II) oxidation. *FEMS Microbiol. Ecol.* **88**, 503–515.
- Wu W., Swanner E. D., Kleinhanns I. C., Schoenberg R., Pan Y. and Kappler A. (2017) Fe isotope fractionation during Fe (II) oxidation by the marine photoferrotoph *Rhodovulum iodolum* in the presence of Si—implications for Precambrian iron formation deposition. *Geochim. Cosmochim. Acta*.

- Zeitvogel F., Burkhardt C. J., Schroepel B., Schmid G., Ingino P. and Obst M. (2017) Comparison of preparation methods of bacterial cell-mineral aggregates for SEM imaging and analysis using the model system of *Acidovorax* sp. BoFeN1. *Geomicrobiol. J.* **34**, 317–327.
- Zheng X. Y., Beard B. L., Reddy T. R., Roden E. E. and Johnson C. M. (2016) Abiologic silicon isotope fractionation between aqueous Si and Fe (III)–Si gel in simulated Archean seawater: implications for Si isotope records in Precambrian sedimentary rocks. *Geochim. Cosmochim. Acta* **187**, 102–122.
- Zhou Z., Latta D. E., Noor N., Thompson A., Borch T. and Scherer M. M. (2018) Fe(II)-catalyzed transformation of organic matter-ferrihydrite coprecipitates: a closer look using Fe isotopes. *Environ. Sci. Technol.* **52**, 11142–11150.

*Associate editor:* Stefan Weyer